

**Quantum Transport Properties and Scattering Mechanisms in Transition Metal
Dichalcogenides**

by

Kraig J. Andrews

Ph.D. Dissertation Prospectus

February 2016

Advisor

ABSTRACT

Quantum Transport Properties and Scattering Mechanisms in Transition Metal Dichalcogenides

by

Kraig J. Andrews

February 2016

Advisor: Dr. Zhixain Zhou

Major: Physics

Degree: Doctor of Philosophy

Two-dimensional materials have garnered much interest since the isolation of graphene. Since then layered materials, such as transition metal dichalcogenides (TMDs) have been studied extensively. However, several key problems have yet to be solved. In this study we propose using methods developed to decrease and minimize contact resistance through a novel approach of 2D/2D contacts and hBN encapsulation to study how the mobility and intrinsic properties are affect by *p*-doping WSe₂ device channels. Preliminary results show contact resistance as low as $0.185 \text{ k}\Omega \cdot \mu\text{m}$ using degenerately doped contacts and field-effect mobilities of $\sim 200 \text{ cm}^2\text{V}^{-1}\text{s}^{-1}$ and $\sim 650 \text{ cm}^2\text{V}^{-1}\text{s}^{-1}$ at $T = 300 \text{ K}$ and $T = 5 \text{ K}$, respectively using this 2D/2D contact hBN encapsulation method. In addition, this method is intended to improve mobility at both room temperature for device applications and at low temperatures ($\sim 4 \text{ K}$) to study the integer quantum hall effect (IQHE) and the corresponding related Shubnikov-de Haas oscillations (SdH) to determine information related to quantum scattering times, effective cyclotron mass, and the geometry of the Fermi surface.

Table of Contents

List of Figures	iv
List of Tables	v
1 Introduction	1
1.1 Early Semiconductors	1
1.2 Graphene as a New Two-dimensional Material	1
1.2.1 Properties of Graphene	1
1.2.2 Band Structure of Graphene	2
1.3 Two-dimensional Materials: Transition Metal Dichalcogenides	3
1.3.1 Band Structures of transition metal dichalcogenidess (TMDs)	3
1.4 Current Challenges in TMDs and Beyond	3
2 Experimental Details	6
2.1 Substrate Preperation	6
2.1.1 Substrate Cleaning	6
2.2 Exfoliation	7
2.3 Device Synthesis	8
2.3.1 PDMS Transfer	8
2.3.2 Polycarbonate Pickup Method	9
2.4 Characterization	10
2.4.1 Optical Characterization	10
2.4.2 AFM Characterization	10
2.5 Device Fabrication	11
2.5.1 Device Design	11
2.5.2 Electron Beam Lithography	11
2.5.3 Metal Deposition	12
2.6 Electrical Measurements and Characterization	12
2.6.1 Measurement Devices	13
3 Intrinsic Channel Properties and Scattering Mechanisms	14
3.1 <i>p</i> -type WSe ₂ Semiconductor Contact Resistance	14
3.2 <i>p</i> -type WSe ₂ Hall Effect Measurements	17
3.3 <i>p</i> -type WSe ₂ Field-Effect Mobility	19
4 Future Works and Conclusion	24
4.1 Integer Quantum Hall Effects	24
4.2 Shubnikov-de Haas Oscillations	26
4.3 Performance Limits in TMDs	26
4.4 Conclusion	26
References	28

List of Figures

1.1	Lattice and band structure of graphene	2
1.2	Hexagonal lattice structure of TMD	3
1.3	Band structures of MoS ₂	4
2.1	Plain wafer	6
2.2	Schematic of Si/SiO ₂ substrate	6
2.3	Photolithography system	6
2.4	Alignment marks at varying magnifications	7
2.5	Exfoliation steps	8
2.6	Transfer stage setup	9
2.7	Optical microscope	10
2.8	AFM setup and AFM cantilever	11
2.9	Scanning electron microscope	12
2.10	Electron beam lithography patterns	12
2.11	Au/Ti deposited on device	13
2.12	Electrical measurement devices	13
3.1	Contact resistance of 0.05% Nb doped WSe ₂ channel device	15
3.2	Contact resistance of 0.5% Nb doped WSe ₂ channel device	16
3.3	Hall effect measurement diagram	18
3.4	Hall measurement data for 0.05% Nb doped WSe ₂ channel	19
3.5	Field-effect mobility measurement configuration	20
3.6	Degenerately doped contacts and lightly doped channel field-effect mobility	22
3.7	Undoped WSe ₂ channel with Nb _{0.005} W _{0.995} Se ₂ contacts	23
4.1	Example data of the Integer Quantum Hall Effect	25

List of Tables

1.1	Band gaps of typical TMDs and other materials	4
3.1	Summary of contact resistances for 0.05% Nb doped WSe ₂ channel	16

Chapter 1

Introduction

1.1 Early Semiconductors

The development of microelectronics revolutionized the world in the latter half of the twentieth century. The term semiconductor, in the sense it is known today, first appears in literature in 1911 [1]. Initially, work on the subject was rather pessimistic. However, in the years following Word War II breakthroughs began shed light on the possible applications and the underlying physics involved, such as the ideas of *intrinsic* and *extrinsic* semiconductors [2, 3, 4, 5].

The history of semiconductors and transistors is a well documented subject. The first transistor was constructed at Bell Labs in 1947 using polycrystalline germanium. Shortly thereafter one was developed using silicon. Throughout the following years, these devices were improved on by replacing polycrystalline with single crystals [6]. Then Jack Kilby demonstrated the first integrated circuit (IC) in 1958, for which he would win the Nobel Prize in physics [7, 8]. The scale of ICs grew rapidly in the subsequent years. Initially only a few transistors could fit on a chip (small-scale integration), in stark contrast to modern-day chips that contains billions of transistors [9, 10]. Growth continued at a rapid pace, but eventually it was realized that some limits, material and integration based, existed in silicon and other commonly used materials [11, 12]. In part, these limitations increased the interest in alternative materials. As a result widespread and renewed interest has led to a breadth information and results on a wide range of materials and their applications.

1.2 Graphene as a New Two-dimensional Material

Layered materials have existed for a long time, and have been studied over the last few centuries [13, 14]. In recent decades the scientific study of graphite (3D) has led to new forms of materials, such as carbon nanotubes (1D) and fullerenes (0D) [15, 16, 17]. However, only more recently have scientists began to understand the potential of such layered materials and their potential technological applications. After attempting unsuccessfully to synthesize few-layer graphite during the 1960s, only around 10-50 layers were able to be synthesized, a breakthrough was finally achieved [16]. This most notably began with the synthesis of monolayer graphene [18].

1.2.1 Properties of Graphene

To date, graphene's properties have been the focus of much research, both theoretical and experimental. It has been one of the primary driving forces in study of 'relativistic' condensed matter physics due to its low dimensionality and its band structure that allows electrons to mimic relativistic particles confirming

the appearance of several relativistic phenomena [19, 20, 21, 22]. In its most basic sense, graphene is composed of a single layer of carbon atoms arranged in two-dimensional honeycomb lattice (see fig. 1.1(a)) It has a Young's modulus of 100 GPa (several times more than steel) with a breaking force that is 13% of its Young's modulus [23, 24]. Its strength is due, in part, to its strong in-plane carbon (C) bonds. In addition, graphene can sustain elastic deformations of 20% due to its two-dimensional nature and it has high pliability [16]. These mechanical properties are of interest because graphene lies in the extreme ranges of many metrics considering its size and dimensionality.

Aside from its mechanical properties, graphene's transport properties were another reason why the material was so appealing. Graphene's mobility is several times that of silicon's (electron mobility $\mu \sim 1400 \text{ cm}^2 \text{V}^{-1} \text{s}^{-1}$, hole mobility $\mu \sim 450 \text{ cm}^2 \text{V}^{-1} \text{s}^{-1}$ at room temperature). Experimental results have shown graphene mobility around $15,000 \text{ cm}^2 \text{V}^{-1} \text{s}^{-1}$ with a potential theoretical limit of $200,000 \text{ cm}^2 \text{V}^{-1} \text{s}^{-1}$ [25, 24, 26]. The upper theoretical limit imposed on mobility is due to scattering, however, these high mobilities are achieved mainly because electrons in graphene act very much like photons in their mobility due to their lack of mass. This enables them to travel sub-micron distances without scattering [27]. In reality, there are other limiting factors that need to be considered such as the quality of graphene and scattering with the substrate, for example.

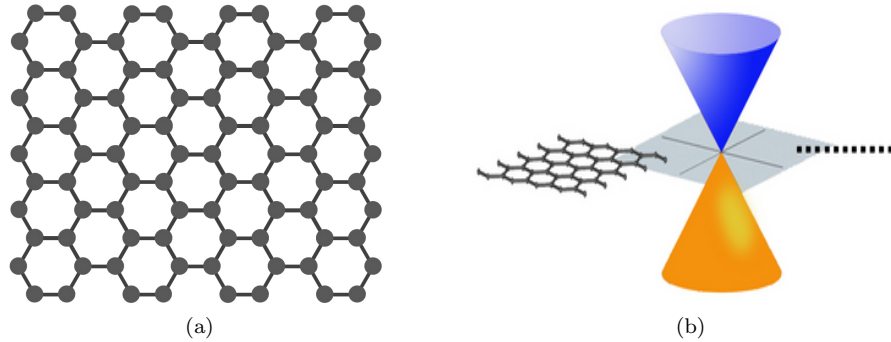


Figure 1.1: (a) Graphene: a layer of carbon atoms in a honeycomb lattice. (b) One of the most unusual features of graphene is that its conduction and valence bands meet at a point, meaning that in single-layer graphene there is no bandgap (Figures obtained from [28]).

1.2.2 Band Structure of Graphene

Despite its impressive properties, the main drawback of graphene is its lack of bandgap. As this became known, the prospect of using graphene for the fabrication to ICs became unlikely. In graphene the conduction and valence bands touch at a single point as shown in fig. 1.1(b) [29]. Ultimately, the lack of a bandgap means that the current on/off ratio is low and is unappealing for logical circuit applications [30]. However, graphene exhibits some interesting properties as a result of having no bandgap, particularly as it pertains to its optical properties. The material's band structure allows for absorption of light over a large range of the electromagnetic spectrum, ranging from infrared ($< 1.65 \text{ eV}$) to ultraviolet ($> 3.2 \text{ eV}$), offering potential electronic-photonic device applications [31, 32, 33]. Since a direct use in logical circuits is not practical researchers have moved on to look for 'two-dimensional materials beyond graphene.' Several attempts at some derivatives of graphene-like materials have been studied, but for the most part they do not seem promising for use in logical circuits [34, 35]. As of late, research has been concentrated on two-dimensional materials, namely transition metal dichalcogenides, as a candidate in ICs and other potential device applications.

1.3 Two-dimensional Materials: Transition Metal Dichalcogenides

Commonly referred to two-dimensional materials beyond graphene, transition metal dichalcogenides (TMDs) have garnered much interest in recent years. TMDs were studied previously, however, they have gained renewed interest due to their properties [36, 37, 38, 39]. TMDs consist of hexagonal layers of metal (M) atoms in between two layers of chalcogen (X) atoms (see fig. 1.2(b)), such that the stoichiometry of the material is MX_2 [30]. The material is dependent on the type of transition metal, typically one of: molybdenum (Mo), tungsten (W), niobium (Nb), rhenium (Re), nickel (Ni), or vanadium (V), and two chalcogen atoms, typically one of: sulfur (S), selenium (Se), or tellurium (Te) [39, 40]. The most commonly studied variations of TMDs are molybdenum disulfide (MoS_2), tungsten diselenide (WSe_2), and tungsten disulfide (WS_2). These materials are commonly stacked together involving van der Waals interactions between adjacent sheets and covalent bonding within each individual sheet (see fig. 1.2(a)) [30]. TMDs have been

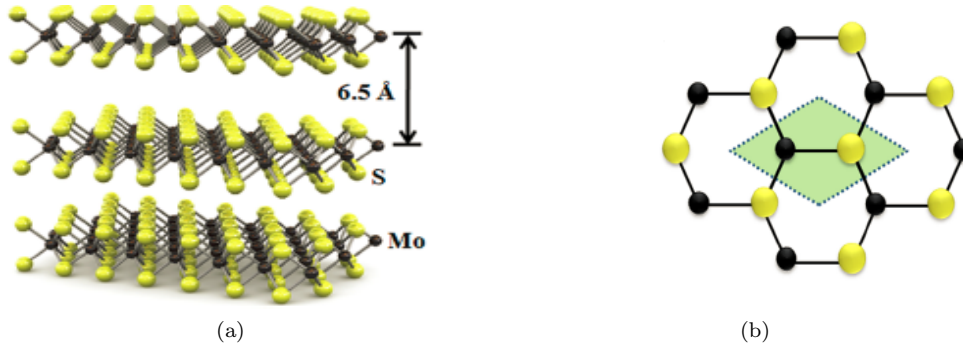


Figure 1.2: (a) The atomic structure of a layered TMD, depicting MoS_2 . Each sheet is composed of three atoms with Mo sandwiched in between two S atoms, S-Mo-S. (b) Top view of a TMD (MoS_2) lattice. (Figures obtained from [41])

found to exhibit a wide variety of interesting properties, including either being a metal or insulator, and displaying the topological insulator effect, superconductivity, and thermoelectricity [42, 43, 44, 45].

1.3.1 Band Structures of TMDs

As stated in sec. 1.2.2, one important property as it pertains to applications for logical circuits is the material's band structure. One of the main reasons TMDs have been so extensively studied lately is due to the fact that, unlike graphene, they do exhibit a bandgap. The bandgaps in some commonly used TMDs is interesting because of the transition from an indirect to a direct bandgap as the layered thickness decreases. Fig. 1.3 illustrates this, for bulk and few-layer MoS_2 there is an indirect band gap while for monolayer MoS_2 there is a direct bandgap. This unusual structure results in some unique optical properties making monolayer TMD promising candidates for optoelectronic devices [46, 47]. Table 1.1 summarizes some TMD bandgap energies that are of considerable interest to the device fabrication process.

1.4 Current Challenges in TMDs and Beyond

There are several challenges facing the advancement of study of TMDs. One of these is the development of low contact resistance devices. The formation of a Schottky barrier (SB) occurs when making electrical contacts [58, 59]. This problem affects many aspects of the growth of TMDs, low contact resistance devices are essential for the study of intrinsic transport properties and performance limits of devices. Two main approaches exist for achieving low-resistance metal-semiconductor contacts. The first of these is lowering the Schottky barrier height (SBH) by choosing metals with proper work functions. Finding metals with the proper work function to minimize the SBH while still maintaining a high conductivity has proven to be



Figure 1.3: Calculated band structures of (a) bulk MoS₂, (b) four-layer MoS₂, (c) bilayer MoS₂, and (d) monolayer MoS₂. Here the solid arrows indicate the lowest energy transitions. (Taken from [48], originally appeared in [49])

2D material	theoretical E_g (eV)	experimental E_g (eV)
graphene	0	0
bilayer graphene	0	0
bulk <i>h</i> -BN	-	5.97 [50]
monolayer <i>h</i> -BN	-	6.07 [51]
few layer (2-5) <i>h</i> -BN	-	5.92 [52]
bulk MoS ₂	1.2 ^{a,b} [53, 54]	1.0-1.29 ^b [53, 54]
monolayer MoS ₂	~ 1.90 ^{a,c} [55]	~ 1.90 ^b [55]
bulk WS ₂	~ 1.30 ^{a,b} [53, 56]	~ 1.35 ^c [53, 56]
monolayer WS ₂	~ 2.10 ^{a,c} [57]	-

^a Theoretical calculations based on first-principles calculations using density functional theory (DFT).

^b Indirect bandgap semiconductor.

^c Direct bandgap semiconductor.

Table 1.1: Summary of the bandgaps of typical monolayer, bilayer, and bulk TMDs and *h*-BN materials. Table adapted from ref. [30].

difficult [60, 61]. If a proper work function metal were to be found that met the requirements for current TMD performance the effect of lowering the SBH may still be diminished due to Fermi level pinning [62]. Therefore, another method to achieve low-resistance contacts is desirable. The second approach used to achieve low-resistance contacts is to degenerately dope the contact regions. Heavily doping the contact region effectively decreases the SB width [63]. However, this too, has its own challenges associated with it. One possible way to overcome the problems and tune the SB is to use a buffer layer and covering with a material such as hBN or graphene [64, 65, 66, 67]. This second approach has shown promise in reducing the contact resistance and lowering the SB while still maintaining high carrier mobility (see ch. 3).

Aside from the commonly used two-dimensional materials like MoS₂ and WSe₂, black phosphorus (BP) has begun to show promise. Bulk BP has a direct bandgap of ~ 0.3 eV, which is expected to increase to ~ 2.0 eV as the thickness approaches monolayer [68, 69, 70]. In the past few years, few-layer black phosphorus has been shown to have desireable room temperature field-effect mobility (~ 1,000 cm²V⁻¹s⁻¹ for ~ 10 layer BP and ~ 200 cm²V⁻¹s⁻¹ for 5 nm BP) [71, 72, 73]. BP has shown potential for applications to thin-film electronics and infrared optoelectronics due to its bandgap energy range [74, 73]. In addition,

the high mobility measurements have recently allowed for measurements of novel quantum physics, opening the door to further study of intrinsic channel properties of TMDs.

Chapter 2

Experimental Details

2.1 Substrate Preparation

Using degenerately doped silicon dioxide (SiO_2) wafers that are 270 nm thick as pictured in fig. 2.1 and the subsequent substrate's schematic in fig. 2.2, there are several preliminary steps needed prior to device fabrication. For easy identification of locations on the substrate alignment marks are placed on the wafer using photolithography (see setup in fig. 2.3). There is a main alignment mark pictured in figs. 2.4(a) and 2.4(b) which allows for quicker identification during electron beam lithography, for example. The alignment marks are in a grid pattern with the coordinate $(0, 0)$ at the center, stretching to $(\pm 6, \pm 6)$ in both the right and left directions. In each of these coordinate locations there smaller alignment marks evenly spaced within them as shown in figs. 2.4(c) and 2.4(d). Next, gold (Au) is deposited on the surface of the wafer, a process that will be explained in more detail in sec. 2.5.



Figure 2.1: Plain, polished uncut Si/SiO_2 wafer.



Figure 2.2: Schematic of Si/SiO_2 substrate.

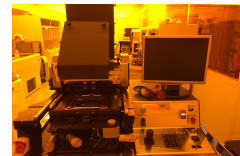


Figure 2.3: Photolithography system for creating alignment marks on substrates.

2.1.1 Substrate Cleaning

First, a SiO_2 wafer is cut to the appropriate size with its preexisting Au layer. To remove the Au layer, the substrate is first soaked in acetone for approximately 5-10 minutes then washed using isopropanol (IPA) and dried with nitrogen (N_2) gas. Next, the substrate is placed in acetone and sonicated for 15 minutes. Then sonicated once more but in IPA this time with a repetition of washing and drying step using IPA and N_2 as described above in between each sonication. In order to remove any remaining organic matter on the surface of the substrate, the substrate is annealed under vacuum at 600°C for 10 minutes and passing forming gas for 2 of the 10 minutes. Forming gas is a mixture of H_2 and an inert gas, usually N_2 [75]. In addition to annealing the substrate for cleanliness, in certain cases when a higher degree of cleanliness is desired the substrate can be treated with oxygen plasma cleaning.

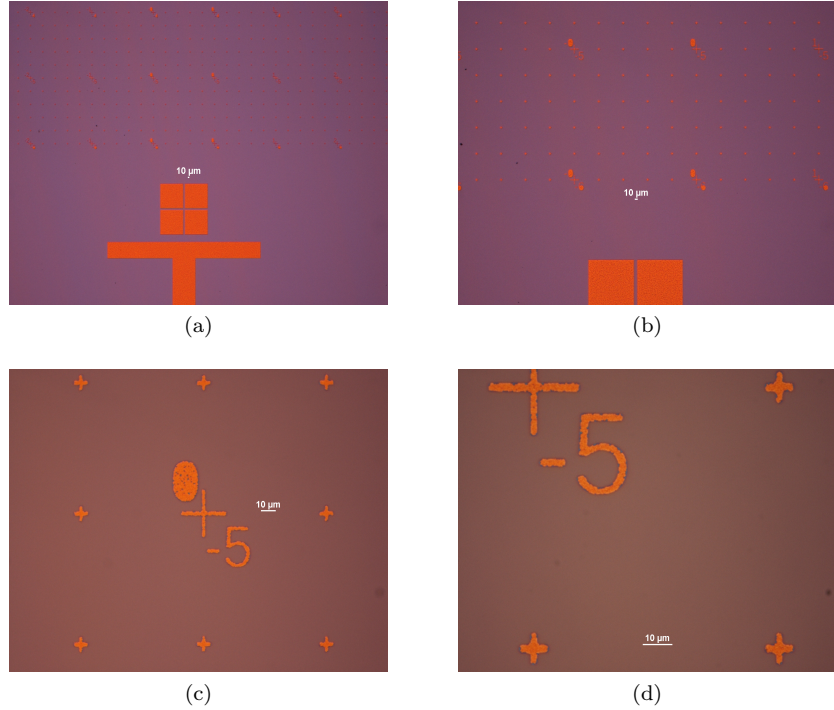


Figure 2.4: (a) Main alignment mark at 5x magnification. (b) Main alignment mark at 10x magnification. (c) Coordinate mark $(0, -5)$ at 50x magnification. (d) Coordinate mark $(0, -5)$ at 100x magnification.

2.2 Exfoliation

To synthesize samples the most common and often most effective method used is mechanical exfoliation, a technique made famous by Novoselov *et al.* [18]. The process involves using Scotch tape to repeatedly cleave layers of MoS₂ or some other TMD. Initially a crystal of a particular TMD (see fig. 2.5(a)) is placed on a piece of Scotch tape (see fig. 2.5(b)). Then taking another piece of tape and pressing in on the crystal that is on the first piece of tape, being sure to press hard and firm on the crystal. The tape is then lifted up and this process is repeated until the whole piece of tape is filled with small samples of the TMD (see fig. 2.5(c)). At the end of this process it is expected that there are a wide range of mixture of sample sizes in terms of area and in term of thickness as well, where thicknesses of < 3 nm are not uncommon. To better characterize the samples the optical microscope is used.

The main challenge that exists with this method is the ability to synthesize a high yield of monolayer samples. This does not seem to be much of a challenge when it comes to graphene and some other TMDs, but with regard to MoS₂ this is not the case. Based on recently published literature in an effort to increase the yield of monolayer MoS₂ various methods and techniques were tested and modified accordingly [76]. In this modified method an additional step to cleaning the substrate is added in which it undergoes oxygen plasma cleaning for 10 minutes to ensure the cleanliness of the substrate's surface. To promote more bonding between the substrate and the samples, the substrate is first heated at 300° C for 10 minutes without any samples on it. During this process the normal cleaving of sample on tape from crystal takes place. Once the substrate is done heating the tape containing the samples is immediately placed on the substrate and pressed firmly for several minutes. Then the substrate (with the tape still on it) is placed on a glass slide (microscope slide) and is heated at around 85° C for five minutes. Next, the substrate (with tape) is removed from heat and the tape slowly peeled back from the substrate. The result should be a much higher yield of < 3 nm samples of larger surface area, and several trilayer, bilayer, and a few

monolayer samples.

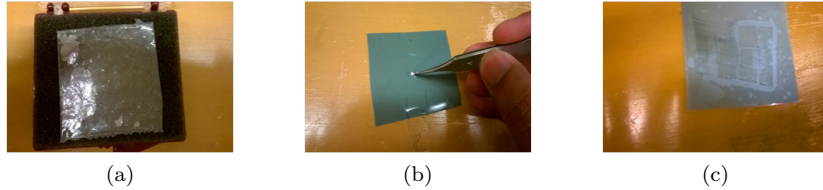


Figure 2.5: (a) Bulk MoS₂ crystal. (b) Single MoS₂ crystal on tape. (c) Tape with exfoliation MoS₂ crystals.

Most commonly SiO₂ substrates are the main items that are exfoliated onto. However, depending on the material being synthesized, this may not always be the case. In cases where samples of hBN or in the event that the thickness of the synthesized sample is not of great importance and can be tolerated up to 20 – 30 nm, polydimethylsiloxane (PDMS) is exfoliated onto instead of SiO₂ substrates. The resulting samples are of varying thickness, on average around 20 nm. Thin samples (usually trilayer and above) can be made using this method of PDMS, however, these samples tend to have small surface area and lack uniformity which poses problems as to their usability. As such, this remains an effective method for obtaining samples in which thickness is not the main concern. Once the samples have been optically characterized, the sample(s) on PDMS must be transferred to a SiO₂ substrate.

2.3 Device Synthesis

Once the sample or samples have been synthesized and characterized for their specific purpose these samples can begin to be synthesized into a device for measurement. Generally, this involves the technique of transfer. Transfer is usually done using the aforementioned PDMS or using polycarbonate (PC) known as the PC pickup method.

2.3.1 PDMS Transfer

PDMS transfer is most useful for samples that were originally exfoliated onto PDMS, for example hBN. To manufacture PDMS a 10:1 ratio of silicone base and curing agent is mixed together and placed in vacuum for 30 minutes to ensure the removal of any remaining air bubbles. After this time the mixture is then spin coated on a plain SiO₂ wafer and heated at 80 °C for 30 minutes then allowed to cool for 30 minutes. Once cooled, the surface of the wafer can be cut using a razor into small stamps that can be used for exfoliation and for transfer.

Once the samples that are to be transferred are on the PDMS stamp, it is placed on a glass slide. The optical microscope is used to locate the sample on the stamp and using a razor to cut small excess pieces from the portions of the stamp where the desired sample is not located. This process is repeated until the size of the cut stamp is now reasonably small. The cut stamp is then placed at the edge of a new glass slide with sample area of the stamp as close to the edge as can be and the other side of the stamp is taped down using Scotch tape.

Next a substrate is placed and secured using glue (usually PMMA) to the stage of the transfer setup. The transfer stage setup is pictured in fig. 2.6. It consists of a microscope that has the capability of 10x or 20x magnification and a micro-manipulator. The micro-manipulator is where the glass slide with the PDMS stamp is placed. Using the manipulator the substrate on the stage is approached and the position

of the stamp is checked and re-checked multiple times using the microscope to ensure correct overlap of the desired portion of the sample(s). Upon reaching the desired position, the glass slide is lowered, but this time there should be a contrast seen which is the overlapping of the glass slide and the substrate. Once the contrast has enveloped the entire sample that was to be transferred then the manipulator can be used to lift up the glass slide. Once the transfer is complete then the substrate should be annealed at 250 °C for 30 minutes in order to remove any residue or organic matter that may have remained during the transfer process.



Figure 2.6: Transfer stage setup

2.3.2 Polycarbonate Pickup Method

The PC pickup method is used for samples that have been exfoliated onto a SiO₂ substrate. Generally these are thinner samples with larger surface area that are not as easily obtained by using the PDMS exfoliation method as described in sec. 2.2. To manufacture the PC 3.0 g of chloroform and 0.18 g of polycarbonate resin are put on a plate shaker for about 60 minutes or until the polycarbonate resin have dissolved into the solution.

Next, the substrate that has the sample that is going to be transferred is taped using double-sided tape to a glass slide facing up. Then using a syringe the PC solution is placed in the substrate and evenly spread across it, being sure to locate the area(s) on the substrate where the sample(s) are located, small pre-cut pieces of PDMS are placed over top of these areas. An outline of the PDMS stamps is cut using a razor and any excess PDMS is carefully torn away. Once only the PDMS strips are remaining on the substrate deionized water (DI) is put under the strips in order to create a hydrophobic surface and to ensure that the strip and PC that is trapped underneath it come off the substrate with relative ease. Each strip is placed on its own glass slide and is gently blown with N₂ gas to remove any excess DI from the surface.

Moving to the transfer stage setup and following the steps described in sec. 2.3.1 with regard to using the transfer stage setup. The only difference at this point to using this method as opposed to PDMS transfer is in the final step of the transfer. Instead of only lowering until the contrast change is shown between the region that is desired to be transferred, with PC transfer the entire PC must be lowered down. This is because the PC will be heated before being lifted up. Lowering all the way ensures that all the PC will be melted. Once lowered all the way, the heating device, which is connected to the stage, should be turned up to 130 °C. Once this temperature is reached, it should be maintained for approximately two minutes to fully melt the PC film. After heating the substrate and lifting up using micro-manipulator the substrate is placed in chloroform and covered for 30-60 minutes. The purpose of this is to remove any

residue left over by the PC film or any other items that may have been introduced at any point in the transfer process. In practice the chloroform soaking generally needs to be repeated several times over a few hours in order to ensure the least amount of remaining residue possible. To confirm the reduction of residue and also characterize the transferred samples an AFM is used.

2.4 Characterization

There are many ways used in modern academia and industry to characterize samples and devices. Some of these methods include scanning tunneling microscopy (STM), transmission electron microscopy (TEM), atomic force microscopy (AFM), and magnetic force microscopy (MFM) [77]. The primary characterization techniques used in this project are AFM and optical characterization.

2.4.1 Optical Characterization

The majority of the optical characterization is carried out using the optical microscope as shown in figs. 2.7(a) and 2.7(b). The microscope can magnify 5x, 10x, 20x, 50x, and 100x, in addition, it can show dark field images.

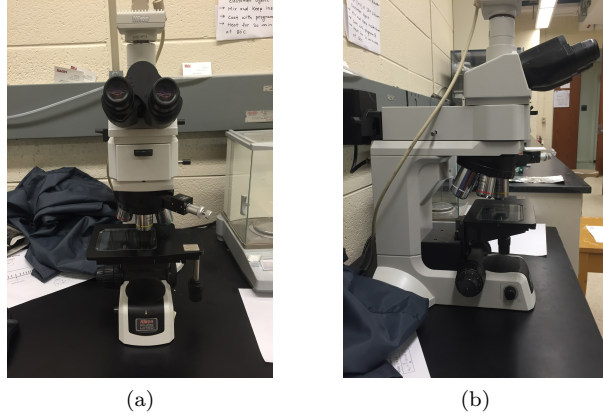


Figure 2.7: (a) Optical microscope front view. (b) Optical microscope side view.

2.4.2 AFM Characterization

In addition to the characterizing samples optically, AFM characterization is another important aspect of the device design and fabrication process. AFM characterization occurs several times throughout the process, after each transfer of a sample onto another, for example. This occurs for two reasons; to verify the thickness of the sample(s) that have been transferred, and also to verify the cleanliness of the surface of the sample (to ensure that any residue has been removed, especially during the course of PC transfer). Additionally, once the electrodes of the device have been fabricated a final AFM characterization is needed to determine the width of the device's channel which is needed to calculate various important electrical properties.

Fig. 2.8(a) shows a front view of the AFM used to characterize. For these purposes, the AFM is operating in “tapping” mode which is less invasive than “contact” mode [77]. In basic terms, an AFM works by measuring the force between the tip of a cantilever (see fig. 2.8(b)) and the sample being imaged.

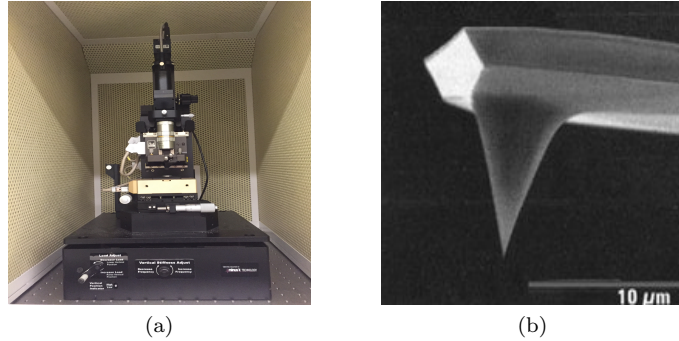


Figure 2.8: (a) Front view of AFM setup. (b) AFM cantilever tip [78].

2.5 Device Fabrication

In order to perform electrical measurements of devices one must fabricate devices with electrodes. The devices are fabricated according to a specific process, though it is worth noting that under certain circumstances some steps of the process may be omitted or altered, however, the main idea remains the same regardless of the device type being fabricated. Once all transfer steps and samples have been placed in their correct locations the fabrication process begins. This process has three main steps: device design (sec. 2.5.1), electron beam lithography (EBL) (sec. 2.5.2), and metal deposition (sec. 2.5.3).

2.5.1 Device Design

The specifics of device electrode design depends largely on the type of measurement that is desired. For example, fig. 2.10(b) demonstrates a Hall bar device pattern. Despite the varying possibilities of patterns, the method for which the designs are generated remains largely the same. In order to generate these patterns a design software, Nanometer Pattern Generation System (NPGS), is used to draw the electrodes which in turn communicates the designed pattern to the SEM [79].

In preparation for EBL the substrate is spin-coated with two layers of polymethyl methacrylate (PMMA). The first layer of PMMA is 495-A4 is added then the substrate is baked on a hot plate for 5 minutes at 180° C. The first layer is followed by another layer of PMMA, 950-A2 (same polymer of different molecular weight). Again, the substrate is spin-coated with this PMMA layer and baked at the same temperature for 5 minutes.

2.5.2 Electron Beam Lithography

To generate the patterns described in sec. 2.5.1 a SEM is used to complete EBL. Fig. 2.9 shows the control panel and electron beam writer of the SEM. The SEM is optimized by adjusting the beam current to the saturation point. Using the alignment marks mentioned in sec. 2.1 the electron beam is aligned to the correct position on the substrate. The NPGS system allows for adjustments in the concentration of the electron beam current at certain areas, for example, whether a line dose or an area dose is necessary. In general, these values are adjusted as needed depending on the device design but are usually around $300 \mu\text{C cm}^{-2}$ for area doses and $15 \mu\text{C cm}^{-1}$ for line doses. Ultimately, the EBL process creates three separate patterns that are joined together. The first pattern is written at 1000x magnification on the SEM (see fig. 2.10(b)). The second and third patterns (written at 300x and 100x, respectively, see fig. 2.10(a)) are connected to the inner 1000x pattern and they connect this inner pattern to the “electrode pads” where the electrodes will eventually be connected for device measurement. After completing the device pattern, the substrate is developed in a solution of methyl isobutyl ketone (MIBK) and methyl ethyl

ketone (MEK) for 70 seconds. The MIBK is the main developer while the MEK acts to enhance the developing process, both fig. 2.10(a) and fig. 2.10(b) have undergone this development process.



Figure 2.9: Control panel and electron beam writer of scanning electron microscope.

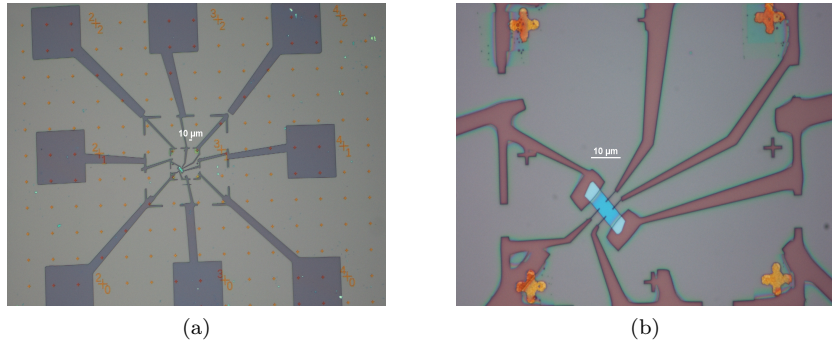


Figure 2.10: (a) Developed pattern at 10x magnification, (b) developed pattern at 100x magnification. Both developed using MIBK and MEK.

2.5.3 Metal Deposition

In order to make proper electrical contacts metal must be deposited on the pattern made by EBL. This process of metal deposition is done using a Bell Jar deposition (BJD) system which evaporates 10 nm of titanium (Ti) followed by 40 nm of Au on the substrate's surface at ultrahigh vacuum ($\sim 10^{-7}$ torr) at a rate of 1 \AA s^{-1} . After the metal deposition process is complete, a process called "lift-off" is performed. In this process the substrate is placed in acetone for approximately 5-10 minutes, until the Au has "lifted-off." Once this process is complete all that remains on the substrate is Au where the EBL was performed. Figs. 2.11(a) and 2.11(b) illustrates a substrate that has undergone the lift-off process, all that remains is the portion of the pattern that is necessary to perform electrical measurements on the device.

2.6 Electrical Measurements and Characterization

Upon completion of the fabrication process and physical characterization processes, the remaining process is electrical characterization. Many of the options available in electrical characterization are put to use, at least in some capacity regardless of the device. Then, depending on the device's quality, further measurements can be made in which a more comprehensive electrical data profile can be obtained.



Figure 2.11: (a) Au/Ti deposited on developed sample after electron beam lithography at 10x. (b) Au/Ti deposited on developed sample after electron beam lithography at 100x.

2.6.1 Measurement Devices

Pictured in fig. 2.12(a) is a measurement device that allows for automated electrical data collection through pre-made programs. The user adjusts parameters and the desired device properties to be measured. Initially, the device is usually measured in non-vacuum conditions at room temperature in order to determine the device's quality. If it is determined that the device's quality is worth continuing with low temperature measurements then the substrate is placed in the vacuum measurement chamber pictured in fig. 2.12(b). This apparatus is used in conjunction with the measurement setup in fig. 2.12(a) to continue measurements. However, in this configuration the measurements take place under ultrahigh vacuum ($\sim 10^{-6}$ to 10^{-7} torr) and temperature control via liquid nitrogen (with the ability to cool to 70 K). In addition, there is another measurement device that allows for both temperature control and the application of a magnetic field. This device, known as a physical property measurement system (PPMS), is shown in fig. 2.12(c) and is used in situations when it is necessary to apply a magnetic field such as measuring a Hall device.

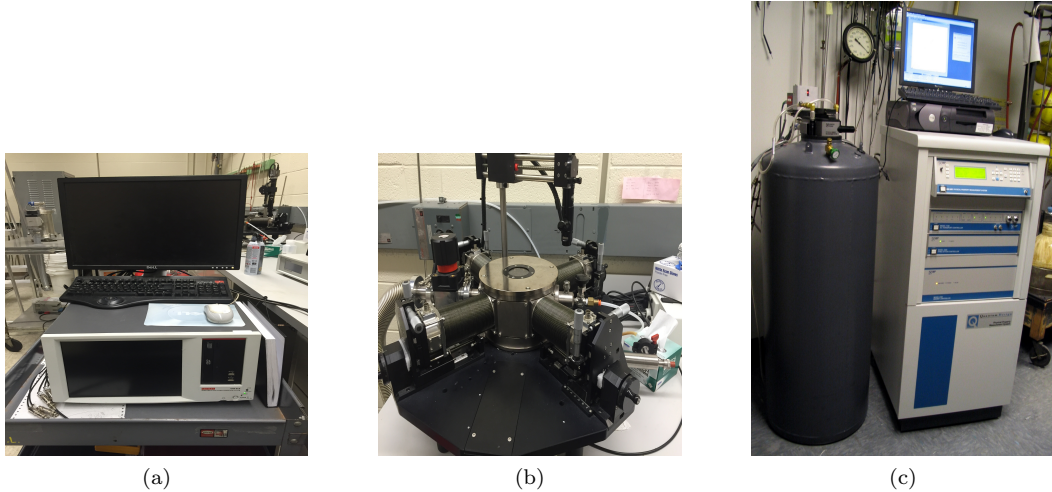


Figure 2.12: (a) Keithley semiconductor measurement system. (b) Low temperature, vacuum measurement chamber. (c) Physical property measurement system.

Chapter 3

Intrinsic Channel Properties and Scattering Mechanisms

Developing low resistance ohmic contacts opens up possibility to study the intrinsic properties of TMDs and quantum physics. In particular, quantum phenomena inherent to two-dimensional electron gass (2DEGs) and two-dimensional hole gass (2DHGs) such as the integer quantum Hall effect (IQHE) and Shubnikov-de Haas (SdH) oscillations can be explored in high mobility monolayer and few-layer TMDs [80]. In addition to quantum transport properties and quantum effects in monolayer and few-layer TMDs the study of mobility and its corresponding temperature dependence can be used to understand the multiple scattering mechanisms present [81]. The study of both electron and hole transport mechanisms is important due to the fact that high-performance *p*-type and *n*-type transistors are necessary for complementary digital applications.

3.1 *p*-type WSe₂ Semiconductor Contact Resistance

One of the major challenges that still remains in fabricating devices to study intrinsic channel properties and scattering mechanisms is developing high quality *p*-type WSe₂ devices. This is due to the fact that the metal/WSe₂ (or MoS₂) interface is obstructed by a large SB formed by the Fermi level pinning close to the conduction band of the WSe₂ [82, 61].

In order to fabricate high quality *p*-type WSe₂ devices, one aspect that must be addressed is how doping affects the SBH. In particular, it is important to determine how doping can improve the contacts in devices. To address this issue of contact resistance several devices were fabricated and characterized in order to determine the contact resistance. Using the transmission line model (TLM) several WSe₂ devices were made with electrodes spaced at varying lengths from the source electrode.

Fig. 3.1(a) illustrates an example of a transmission line device that was used to characterize the contact resistance. The device shown has a 0.05% Nb doped WSe₂ channel. The resistance in general is given by

$$R = \frac{\rho}{A} l, \quad (3.1)$$

where, in this case, it is assumed that the resistivity ρ and the area A are constant throughout the device [83]. The resistance R is then proportional to the length l . By determining the resistance as a function of length one can determine the contact resistance of the device. The total resistance is given by

$$R = R_{ch} + 2R_c, \quad (3.2)$$

where R_c and R_{ch} are the contact and channel resistances, respectively [83]. Thus by finding the resistance from the gradient of an I-V characteristic curve, one can apply the logic from eqs. 3.1 and 3.2 to find the contact resistance. Using this method the resistance as a function of length is shown in figs. 3.1(b),

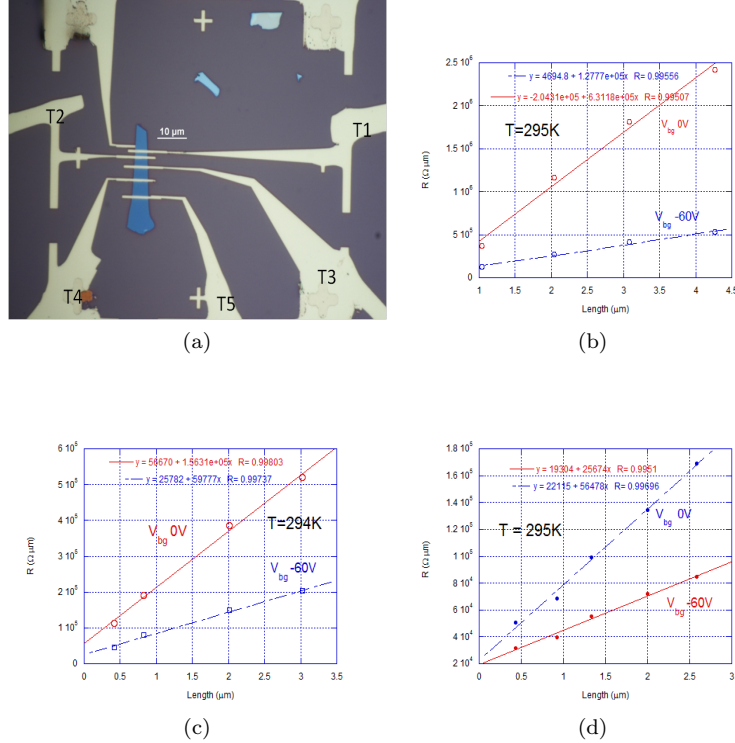


Figure 3.1: (a) 0.05% Nb doped WSe₂ channel transmission lines with corresponding channel lengths and widths of $L_{12} = 1.04\text{ }\mu\text{m}$, $W_{12} = 4.42\text{ }\mu\text{m}$, $L_{23} = 2.04\text{ }\mu\text{m}$, $W_{23} = 4.47\text{ }\mu\text{m}$, $L_{34} = 3.09\text{ }\mu\text{m}$, $W_{34} = 4.90\text{ }\mu\text{m}$, $W_{45} = 5.15\text{ }\mu\text{m}$, and $L_{45} = 4.27\text{ }\mu\text{m}$. (b)-(d) show the resistance $R(\Omega \cdot \mu\text{m})$ as a function of L , where the contact resistance is found by using a linear fit function. The fits were performed at $T = 295\text{ K}$ for V_{bg} of 0 V and -60 V . Note that (b) refers to the device shown in fig. (a).

3.1(c), and 3.1(d) for both $V_{bg} = 0\text{ V}$ and $V_{bg} = -60\text{ V}$. From these figures one can interpret the contact resistance of the device as the intercept value with the value, the resulting contact resistances are summarized in table 3.1. The results show linear behavior at room temperature for both backgate voltage of $V_{bg} = 0\text{ V}$ and $V_{bg} = -60\text{ V}$. The reported resistance values are larger for lower V_{bg} measurements, this can be explained by the energy mismatch of Fermi levels between the metal contacts and the lightly doped WSe₂. As the backgate voltage is increased from $V_{bg} = 0\text{ V}$ to -60 V the SB that is present in the contacts has narrowed and as a result of the increased V_{bg} there is more transport across the barrier. The relatively small contact resistance of $2.35\text{ k}\Omega \cdot \mu\text{m}$ indicates that low resistance contacts can be achieved at sufficiently high backgate voltage. The contact resistances are on the same order of magnitude measured by Cui *et al.* at $T = 300\text{ K}$ at a relatively high backgate voltage ($\sim 0.7 - 10\text{ }\Omega \cdot \mu\text{m}$) [80].

In light of this result, the addition of degenerately doped contacts (like those fabricated in sec. 3.3) could further improve the contact resistance. By adding 0.5% Nb doped WSe₂ contacts, for example, the Fermi level energy mismatch between the metal and the degenerately doped WSe₂ contact would be decreased, thereby lowering the SBH and coupled with sufficiently high backgate voltage, the ability to achieve $< 1\text{ k}\Omega \cdot \mu\text{m}$ contact resistance is plausible.

For comparison, using degenerately Nb doped (0.5%) WSe₂ channel the contact resistance can be significantly reduced. Table 3.1 summarizes the contact resistance for the degenerately doped and lightly doped contacts. Figs. 3.2(b) and 3.2(c) show the normalized resistance as a function of channel length at both $T = 295$ K and $T = 5$ K. The fact that the contact resistance is still $< 0.2 \text{ k}\Omega \cdot \mu\text{m}$ shows that the contacts are desirable. As the temperature is decreased, usually the contact resistance becomes larger (mostly due to the lack of thermionic emission over the barrier), however, this is not the case here. These results with degenerately doped contacts point towards this method as being a suitable way to fabricate low-resistance devices especially at low temperatures.

Doping content of Nb	$R_c (\text{k}\Omega \cdot \mu\text{m})$
0.05%	2.35 ^a
0.05%	12.9 ^b
0.05%	9.65 ^c
0.5%	0.195 ^d
0.5%	0.185 ^e

^a Resistance values from fig. 3.1(b).

^b Resistance values from fig. 3.1(c).

^c Resistance values from fig. 3.1(d).

^d Resistance values from fig. 3.2(b).

^e Resistance values from fig. 3.2(c).

Table 3.1: Summary of contact resistances for 0.05% Nb doped WSe₂ channel found using linear fit data from figs. 3.1(b), 3.1(c), 3.1(d), 3.2(b), and 3.2(c).

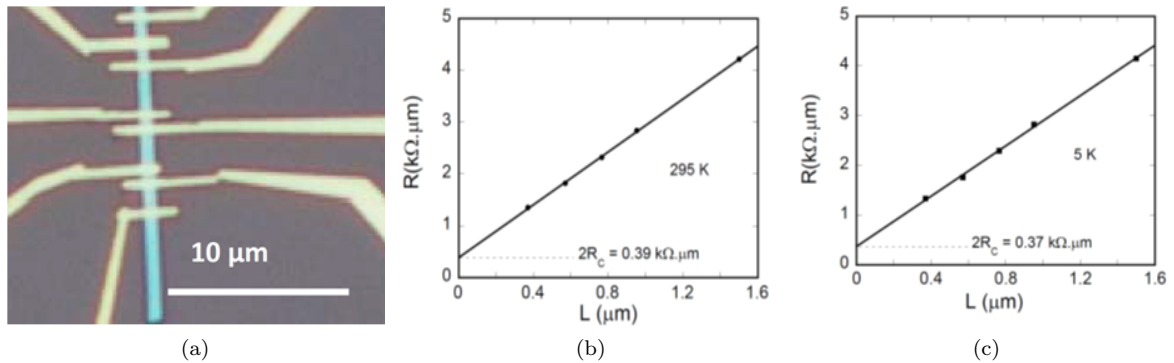


Figure 3.2: (a) Device structure for TLM measurement consisting of a ~ 18 nm thick degenerately *p*-doped WSe₂ device with Ti/Au metal contacts. (b) Normalized total resistance as a function of channel length measured at room temperature $T = 295$ K and (c) low temperature $T = 5$ K. (Figure appeared in [84])

3.2 *p*-type WSe₂ Hall Effect Measurements

In addition to knowing how doping can be used to lower the SBH, doping also affects the intrinsic channel properties. To study how these properties are effected several measurements were taken. First, Hall bar devices were fabricated. These devices were similar to those used in sec. 3.1, the channel was doped with the same amount of Nb. The only differing aspect of these devices was the electrode design. Fig. 3.4(a) shows an example of one such Hall bar device.

The Hall effect measurement is widely used for semiconductor characterization as it gives useful electrical properties such as the resistivity, carrier density, and mobility [83]. Consider the setup shown in fig. 3.3, where the length L is taken in the x -direction, width w in the y -direction, thickness t in the z direction, and e denotes a charge carrier which can be either an electron or a hole. The current I flows in the positive x -direction and is given by

$$I = Jwt = nev_x wt, \quad (3.3)$$

where J is the current density in the x -direction, n is the charge carrier number density, and v_x is the charge carrier drift velocity in the positive x -direction. The current I is a result of the application of an electric field E along the positive x -direction. In the presence of a magnetic field B in the positive z direction the charge carriers will experience a Lorentz force that deflects them toward one side of the device. As a result there is an accumulation of charges alone one side of the device which in turn creates a transverse electric field E_y [85]. The transverse electric field E_y is given by

$$E_y = v_x B, \quad (3.4)$$

where B is the magnetic field in the z direction. This accumulation of charges along one side of the device creates a potential difference that is related to the transverse electric field E_y and can easily be used to find the Hall voltage V_H by

$$V_H = - \int_0^w E_y dy = -E_y w. \quad (3.5)$$

Finally, by combining eqs. 3.3, 3.4, and 3.5 a final expression for the Hall voltage V_H is given by

$$V_H = -\frac{IB}{t} \left(\frac{1}{ne} \right). \quad (3.6)$$

From eq. 3.6 two forms of the Hall coefficient become evident,

$$R_H = \frac{1}{ne} = \frac{V_H t}{IB}. \quad (3.7)$$

Since e refers to either holes or electrons, the sign of R_H would also vary in accord with the proper carrier being described in the circumstance. Furthermore the conductivity is given by

$$\sigma = ne\mu_H, \quad (3.8)$$

where σ is the conductivity and μ_H denotes the Hall mobility. Thus, an expression for the Hall mobility can be found by combining eqs. 3.7 and 3.8 to give

$$\mu_H = |R_H| \sigma = \frac{\sigma V_H t}{IB}. \quad (3.9)$$

Following this prescribed method the Hall mobility μ_H and charge carrier density for lightly doped channel WSe₂ devices were found.

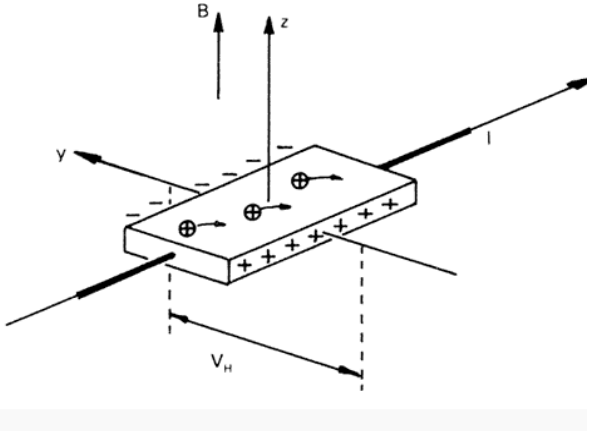


Figure 3.3: Geometry of Hall effect measurement. Current flows in the positive x -direction and magnetic field is applied in the positive z direction generating a Hall voltage [86]. Diagram originally appeared in ref. [87].

Fig. 3.4(b) illustrates IV characteristics for the device pictured in fig. 3.4(a) for V_{bg} ranging from -70 V to 20 V at $T = 300$ K. The linear behavior implies that the contacts exhibit ohmic behavior. Fig. 3.4(c) shows the conductivity σ as a function of V_{bg} for various temperatures. Since conductivity is proportional to charge carrier density, which is in turn proportional to the backgate voltage, one would expect to see the behavior shown here. As the temperature increases one notices that the conductivity also increases. This is not ideal behavior, as temperature is increased one would expect the conductivity to decrease. The fact that the opposite of this is observed can be attributed to a number of reasons. The device in question is subject to interface scattering as it is on the Si/SiO₂ substrate (ideally a hBN substrate would be used here to decrease the interface scattering), there is increased charge impurity scattering from doping the channel, and also metal to semiconductor contacts exhibit a high contact resistance as there is no method employed here to lower the SBH. Overall, this observed behavior in the conductivity points to a barrier that has developed. Conductivity ranges from $\sigma \sim 12 \mu\text{S}$ at $T = 300$ K to $\sim 5 \mu\text{S}$ at $T = 180$ K, both at $V_{bg} = -80$ V. In addition to the conductivity increasing with temperature, so too, does the Hall mobility μ_H . This fact is shown in fig. 3.4(d).

The Hall mobility as a function of temperature for charge carrier densities $n = -3.5 \times 10^{-7} \text{ C cm}^{-2}$ and $n = -2.5 \times 10^{-7} \text{ C cm}^{-2}$ is shown in fig. 3.4(e). As charge carrier density is increased through the increase of V_{bg} the mobility μ_H increases due to the introduction of more carriers. Fig. 3.4(f) shows the charge carrier density n as a function of V_{bg} for several temperatures. In principle, the carrier density for a given V_{bg} should be the same across all temperatures, however, here there is some discrepancy. This difference could be due to a number of factors; channel doping, contact resistance, the fact that the device's channel was not encapsulated, or some other reason.

The Hall mobilities obtained in this measurement range from $\mu_H = 31.9 \text{ cm}^2 \text{V}^{-1} \text{s}^{-1}$ at $T = 300$ K to $16.7 \text{ cm}^2 \text{V}^{-1} \text{s}^{-1}$ at $T = 180$ K. These values are considerably lower than recent values reported in Pradhan *et al.*, Hall mobilities at same temperature range were all at least an order of magnitude higher [88]. Additionally, other recent results have shown higher Hall mobilities, reaching $34,000 \text{ cm}^2 \text{V}^{-1} \text{s}^{-1}$ in MoS₂ using the hBN encapsulation method and MoS₂ along with graphene-MoS₂ contacts [74]. Overall, these results suggest that the Hall mobility can be greatly improved by implementing a new contact approach (described in sec. 3.1) and encapsulating the channel in hBN (described and results shown in

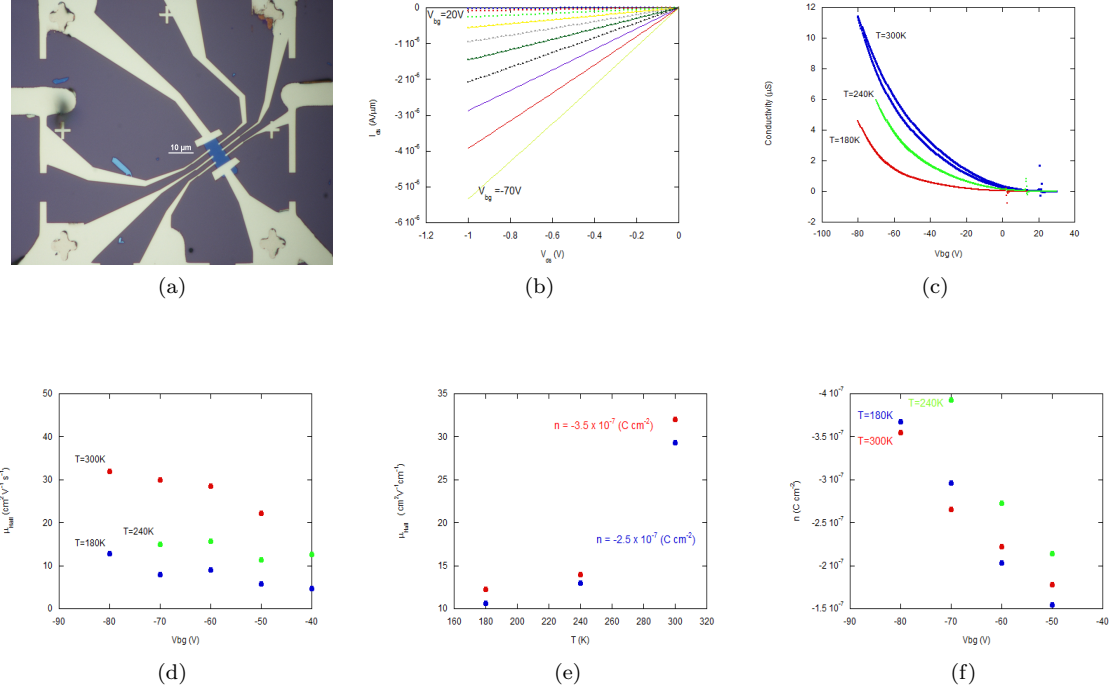


Figure 3.4: (a) Hall bar device with 0.05% Nb doped WSe₂ channel. Sample thickness is 7.74 nm with an average width $W_{avg} = 5.74 \mu m$. (b) IV characteristic curves at $T = 300K$ for V_{bg} ranging from $-70 V$ to $20 V$. (c) Conductivity as a function of V_{bg} for various temperatures. (d) Hall mobility as a function of V_{bg} for various temperatures. (e) Hall mobility as a function of temperature for different charge carrier densities. Carrier densities shown here are calculated at $V_{bg} = -80 V$. (f) Charge carrier density as a function of V_{bg} for various temperatures.

sec. 3.3).

3.3 *p*-type WSe₂ Field-Effect Mobility

In an effort to improve on the approaches and results described in secs. 3.1 and 3.2 a new design of device was fabricated. These devices used a 0.01% Nb doped WSe₂ (lightly doped)channel with 0.5%Nb doped WSe₂ (degenerately doped) contacts. The device fabrication process involved transferring hBN to a Si/SiO₂ substrate then transferring the *p*-doped WSe₂ on top of the bottom hBN creating the channel (see fig. 3.6(a)). Once the *p*-doped WSe₂ is on the bottom hBN substrate then another layer of hBN is transferred to cover the channel (see fig. 3.6(b)). Next, the degenerately doped WSe₂ contacts are transferred onto the device (see fig. 3.6(c)). Finally, the electrodes are designed and the usual device fabrication steps ensue, fig. 3.6(d) shows an example of a measurement-ready device. The main quantity of interest here is the field-effect mobility as it allows for analysis of the device's quality and also allows for a determination of the possible scattering mechanisms present. The two-probe field-effect mobility is given by

$$\mu_{FE} = \frac{L}{w} \frac{dI_{ds}}{dV_{bg}} \frac{1}{C} \frac{1}{V_{ds}}, \quad (3.10)$$

where L is the length of the channel, w is the width of the channel, I_{ds} is the drain current, V_{bg} is the backgate voltage, C is the capacitance, and V_{ds} is the drain voltage [89]. The capacitance is dependent largely on the substrate used, generally Si/SiO₂ and can vary from substrate to substrate as a result the field-effect mobility can vary slightly depending on the capacitance of the substrate.

Initially, the IV characteristics for the device in fig. 3.6(d) show ohmic contacts at $T = 300\text{ K}$, how-

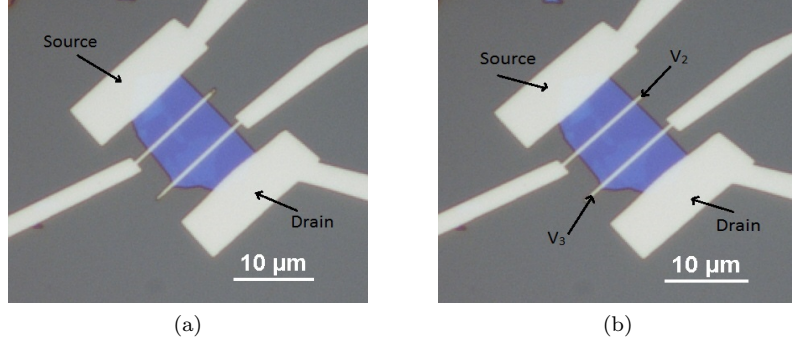


Figure 3.5: Examples of (a) two-point probe measurement configuration for field-effect mobility measurements and (b) four-point probe configuration.

ever, at lower temperatures the contacts are less ohmic. Fig. 3.6(e) shows the linearity expected for various V_{bg} at $T = 300\text{ K}$, but one can see that in fig. 3.6(f) there is a deviation in the linearity that is expected of ohmic contacts. This deviation from ohmic contacts at lower temperatures explains the behavior shown in fig. (g) where the field-effect mobility is degraded at lower temperatures ($T < 80\text{ K}$). In attempt to improve the contacts at lower temperatures the device was annealed at 250 °C for 30 minutes. The result is improved contacts at lower temperatures, fig. 3.6(i) exhibits the linearity expected of ohmic contacts for $T = 10\text{ K}$. Annealing removed any residue or absorbant that may have degraded the contact interface. This result is supported by Britton *et al.* in which annealing improved the mobility, particularly at lower temperatures [90]. The PDMS transfer method, while relatively clean as compared to other available transfer methods, still has the potential to introduce surface residues that can affect the overall device performance, however, it has been shown that while they cannot be eliminated completely, annealing can remove them to some degree and improve device mobility. This change improved the field-effect mobility shown in fig. 3.6(j) where the mobility is not degraded for either V_{ds} and the overall values for mobility improved after annealing. The field-effect mobility shown here is comparable to the results found in Pradhan *et al.* where they observed field-effect mobility values as high as 350 cm²V⁻¹s⁻¹ at $T = 300\text{ K}$ and a maximum field-effect mobility of 650 cm²V⁻¹s⁻¹ for temperature values below $T = 150\text{ K}$ for a *p*-doped WSe₂ device on a Si/SiO₂ substrate [88]. The variation among data sets can be attributed to a number of factors; mainly doping concentration and the device fabrication method.

The field-effect mobility in figs. 3.6(g) and 3.6(j) increases with decreasing temperature which is expected behavior. The At high temperatures the mobility is largely dominated by phonon scattering which is decreased with temperature. At lower temperatures phonon scattering is decreased compared to room temperature measurements and thus long-range Coulomb scattering and short-range atomic defects play a large role [91]. Another possible scattering mechanism is interface scattering or surface roughness scattering. However, the use of a hBN substrate as opposed to a Si/SiO₂ can minimize this scattering mechanism significantly. Channel defects are another source of scattering present in this device. This is largely due to the doping of the WSe₂ channel which introduces impurities that degrades the mobility across all temperatures.

In summary, the improved mobility due to the fabrication of a lightly doped channel and using degenerately doped contacts provides stepping-stone toward further refined devices. However, this technique is challenging because as doping decreases the contact resistance, it increases the channel scattering. In order to fully understand the balance and relationship between doping and the trade-off with scattering mechanisms further study of various doping strengths is needed. With such devices it will become possible to explore the intrinsic property limits of TMDs.

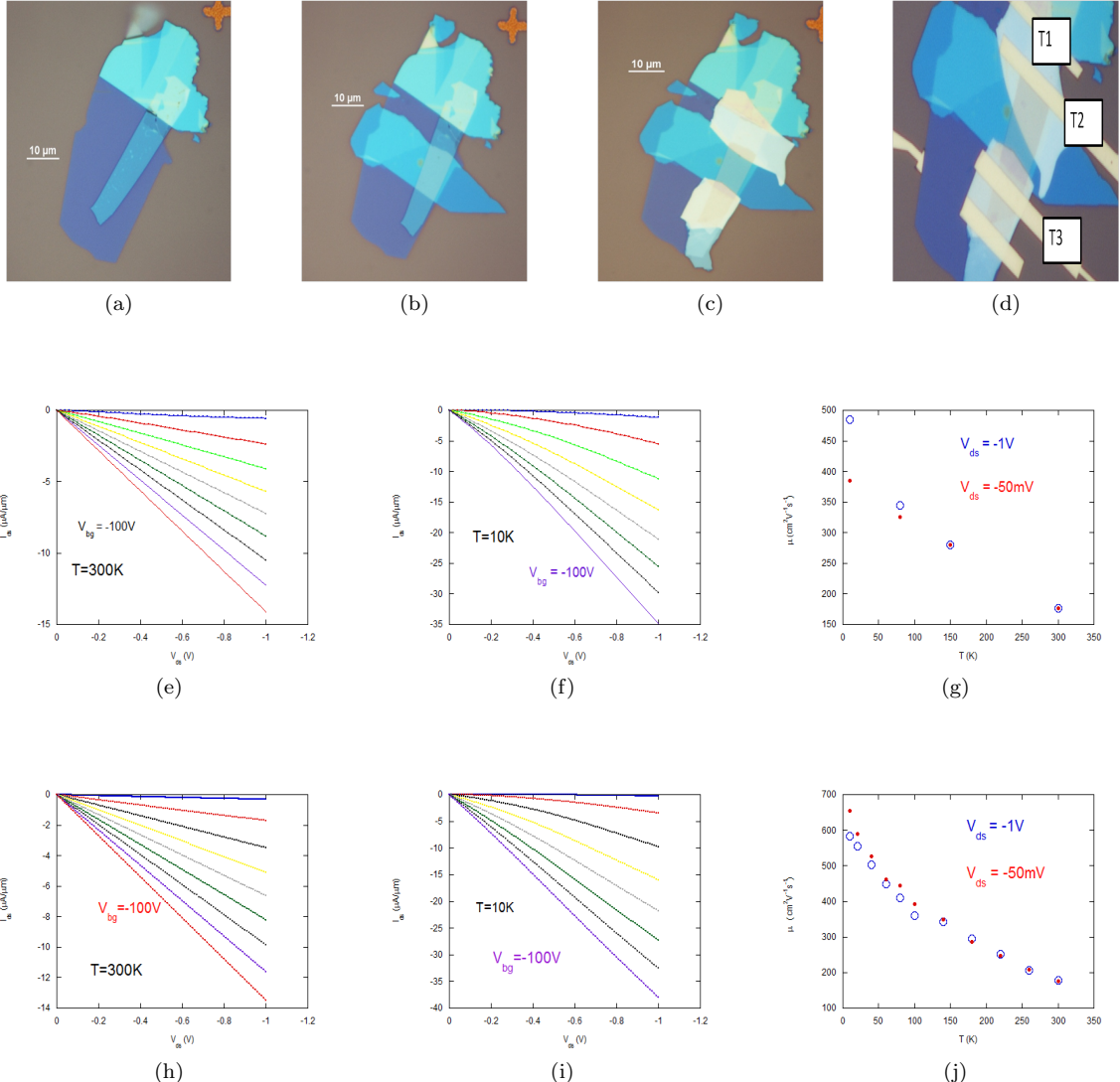


Figure 3.6: (a) 0.01% Nb doped WSe₂ transferred to hBN substrate. (b) Top hBN transferred on WSe₂ channel. (c) Degenerately doped (0.5% Nb doped WSe₂) contacts transferred. (d) Device with 0.01% Nb doped WSe₂ channel and 0.5% Nb doped WSe₂ contacts with electrodes fabricated. Channel dimensions: $L = 12.9\text{ }\mu\text{m}$ and $W = 7.5\text{ }\mu\text{m}$ with a device thickness of 5.6 nm. (e) IV characteristic curves for V_{bg} ranging from -100 V to -20 V at $T = 300\text{ K}$ before annealing the device. (f) IV characteristic curves for V_{bg} ranging from -100 V to -20 V at $T = 10\text{ K}$ before annealing the device. (g) Two-probe field-effect mobility as a function of temperature for $V_{ds} = -50\text{ mV}$ and $V_{ds} = -1\text{ V}$ before annealing the device. (h) IV characteristic curves for V_{bg} ranging from -100 V to -20 V at $T = 300\text{ K}$ after annealing the device for 30 minutes at 250° C . (i) IV characteristic curves for V_{bg} ranging from -100 V to -20 V at $T = 10\text{ K}$ after annealing the device for 30 minutes at 250° C . (j) Two-probe field-effect mobility as a function of temperature for $V_{ds} = -50\text{ mV}$ and $V_{ds} = -1\text{ V}$ after annealing the device for 30 minutes at 250° C .

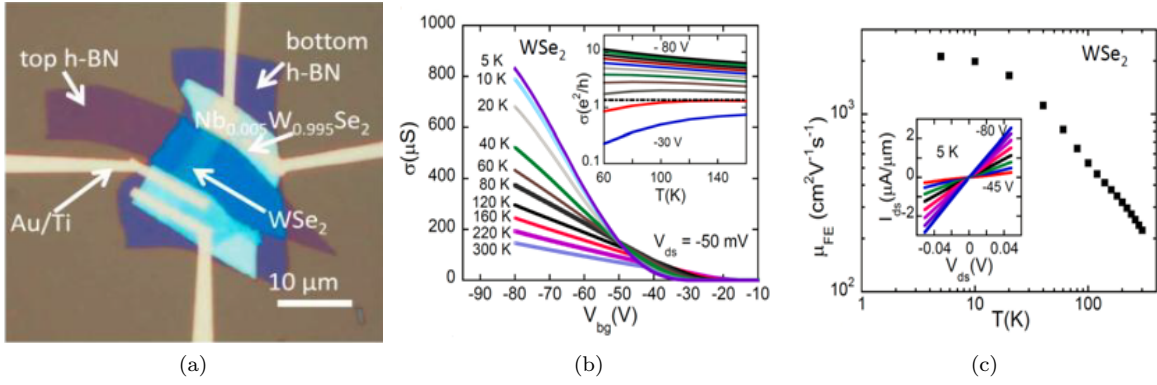


Figure 3.7: (a) Optical image of the WSe₂ FET with degenerately doped contacts (Nb_{0.005}W_{0.995}Se₂). Channel WSe₂ is encapsulated in hBN. The WSe₂ channel is ~ 3.5 nm thick, 14.8 μ m long, and 4.7 μ m wide. (b) Temperature-dependent two-terminal conductivity of WSe₂ as a function of V_{bg} at $V_{ds} = -50$ mV. *Inset:* temperature dependence of conductivity at varying gate voltages. (c) Two-terminal field-effect hole mobilities in WSe₂. *Inset* Linearity of the output characteristics. (Figures originally appeared in [84])

Chapter 4

Future Works and Conclusion

Certain measurable quantities are valued because of the information they reveal about the geometry of the Fermi surface. Additionally, these quantities are attractive because they depend only on universal constants, experimentally controlled variables, and information about the electronic band structure which is entirely determined by the shape of the Fermi surface [92]. These measurable quantities commonly arise in the presence of a strong magnetic field and low temperature system. Determining the Fermi surface geometry provides insight into the transport and scattering properties of the material.

4.1 Integer Quantum Hall Effects

In a two-dimensional electron system (2DES) there are a number of interesting phenomena that occurs at low temperatures in the presence of strong magnetic fields. One such effect is the IQHE. The IQHE was discovered in 1980 by Klitzing *et al.* [93]. They showed that under a quantum regime of temperature and magnetic field there is a quantization of the Hall resistance, which deviates from its linearity in the magnetic field seen in the classical Hall effect, displaying plateaus at particular values of the magnetic field where the Hall resistance is given purely in terms of universal constants. In addition, the plateaus observed in the Hall resistance are accompanied by a vanishing longitudinal resistance [93, 91, 94, 95].

In order to fully mathematically describe the theory behind the IQHE one must first introduce the concept of Landau levels. Here we assume a quantum regime in which there is a low temperature and high magnetic field such that $\hbar\omega \gg k_B T$. The Hamiltonian of a particle in a uniform magnetic field is given by

$$\hat{H} = \frac{1}{2m} (\hat{p}_x + eBy/c)^2 + \frac{\hat{p}_y^2}{2m} + \frac{\hat{p}_z^2}{2m} - (\mu/s) \hat{s}_z B, \quad (4.1)$$

where \hat{p}_i is the momentum operator in the specified coordinate direction, B is the magnetic field, e is the charge of an electron, $(\mu/s) \hat{s}_z$ is the intrinsic magnetic moment operator [96]. It is worth noting that the vector potential chosen in eq. 4.1 is known as the Landau gauge, $\vec{A} = (-By, 0, 0)$, which implies the magnetic field B is directed in the positive z -direction [97, 98]. In this case the eigenfunctions of the Hamiltonian must take the form,

$$\psi(\vec{r}) = e^{(i/\hbar)(p_x x + p_z z)} \chi(y), \quad (4.2)$$

where $\chi(y)$ is defined by solutions to

$$\frac{\partial^2 \chi}{\partial y^2} + \frac{2m}{\hbar^2} \left[E + (\mu/s) \sigma B - \frac{p_z^2}{2m} - \frac{1}{2} m \left(\frac{eB}{mc} \right)^2 (y - y_0)^2 \right] \chi = 0, \quad (4.3)$$

where $y_0 = -cp_x/eB$ and $\omega = |e|B/mc$. Additionally, since the Hamiltonian does not explicitly depend on x and z this implies that both the x and z components of the generalized momentum are conserved.

Eq. 4.3 is formally identical to that of the linear oscillator, thus the expression for the energy levels of a particle in a uniform magnetic field is

$$E = \left(n + \frac{1}{2} \right) \frac{|e|\hbar B}{mc} + \frac{p_z^2}{2m} - (\mu/s) \sigma B, \quad (4.4)$$

where n is any integer [96]. These quantum numbers n specify states known as Landau levels. For the case in which the motion of particles is restricted to a rectangular geometry of $L_x \times L_y$, also let $p_z = 0$ as the motion of particles is restricted in this case to only the $x - y$ plane. In this case the energy of each Landau level is given by

$$E = \left(n + \frac{1}{2} \right) \frac{|e|\hbar B}{mc} - (\mu/s) \sigma B. \quad (4.5)$$

Due to the restriction that $\hbar\omega \gg k_B T$, thermal excitations can be neglected because the interval between Landau levels is much greater than thermal excitation energy. As a result, the probability that electrons will be thermally excited to higher energy levels can be neglected. In order to fill higher energy levels the density of states must be increased. When the Landau level is fully occupied from the lowest to the i th energy level the transverse resistivity becomes

$$\rho_{xy} = \frac{h}{ie^2}, \quad (4.6)$$

where i is any integer corresponding to a specific filled Landau level, e is the charge of an electron, and h is Planck's constant [93, 94]. Eq. 4.6 shows that at critical values of the field, the Hall resistivity (or conductivity) is quantized in units of h/e^2 [77, 95]. Fig. 4.1 demonstrates an example of the quantized

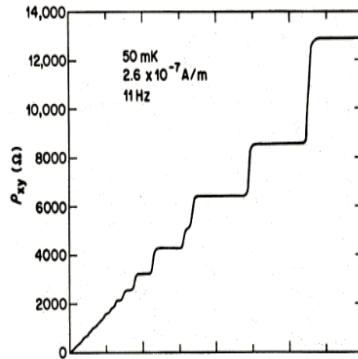


Figure 4.1: ρ_{xy} as a function of magnetic field B at low temperature ($T = 50$ mK). Figure originally appeared in ref. [99].

nature of the transverse resistivity. The distance between each plateau (step height) is given by h/e^2 divided by an integer i . These steplike increases with plateaus in the magnetic field region where the longitudinal resistivity ρ_{xx} vanished [100]. Thus, when $\rho_{xx} = 0$ then $\rho_{xy} = h/ie^2$ and is at a plateau. Note that the temperatures needed to observe the IQHE ($\lesssim 4$ K) is a likely reason why it was not discovered until 1980. It is also important to note that the value of resistivity only depends on fundamental constants of physics and can be used as a primary resistance standard known as the von Klitzing constant, $R_{K-90} = 25812.807 \Omega$ [93, 101, 102]. Observation of the IQHE confirms the high-quality nature of the device in question as it is necessary to obtain high mobilities at very low temperatures. Furthermore, this would offer a more complete picture of the quantum structure of under the high-field limit and allow for the measurement of further quantum properties that reveal important information about the underlying structure of the device.

4.2 Shubnikov-de Haas Oscillations

There are several techniques and measurements that can determine the geometry of the Fermi surface, many of these are closely related to one another and are based on the same underlying mechanism. One such effect is the SdH effect [103]. The SdH effect is an oscillatory dependence of the resistivity on the magnetic field, there it is related to the quantum hall effect (QHE) [104]. This effect is produced by the oscillation of the density of states at the Fermi level which is caused by the quantization of electron energy levels in the presence of a magnetic field (see sec. 4.1, Landau levels) [105, 106]. The oscillations occur with a periodicity of B^{-1} [107].

SdH oscillations can provide a wealth of information about the effective 2DEG (2DHG). For example, one can extract the carrier lifetimes, effective cyclotron mass, information about the Fermi surface [74]. In order to observe the QHE and therefore observe SdH oscillations, high device mobility is required [108, 109]. Recently the Cui *et al.* observed the first SdH oscillations in MoS₂, Li *et al.* and Gillgren *et al.* observed this same effect in black phosphorus (and phosphorene) [80, 74, 110]. Cui *et al.* were able to determine geometry of the Fermi surface from the oscillation frequency and prove the two-dimensional nature of their system. Furthermore, from the analysis of the oscillation amplitude the cyclotron effective masses of both electrons and holes could be determined. From this method the carrier lifetime could also be determined, they reported lifetimes of $\tau = 0.11$ ps and $\tau = 0.12$ ps for holes and electrons, respectively [74, 107]. Cui *et al.* was able to provide insight about the quantum lifetimes and the underlying interactions between short-range and long-range scattering limits [80]. The results provide promise that with the implementations of improvements in contact resistance reduction and further mobility enhancement that the world of TMDs is closer to the routine study of novel quantum physics in two-dimensional systems.

4.3 Performance Limits in TMDs

The ultimate performance limit of TMDs is of interest, especially at room temperature as this is most relevant to device applications. First principles calculations show mobility in monolayer MoS₂ to be $\sim 320 - 410 \text{ cm}^2 \text{V}^{-1} \text{s}^{-1}$ at room temperature depending on initial parameters [111, 81]. Previously the experimental values reported differed by an order of magnitude compared to first principles calculations, however, the improvements made in the area of reducing contact resistance has improved mobility measurements [112, 113]. Experimentally, room temperature mobility measurements of both *p* and *n* type semiconductors still lag behind the theoretical calculations. For example, WSe₂ room temperature mobilities have been reported as $\sim 200 \text{ cm}^2 \text{V}^{-1} \text{s}^{-1}$ with perfect subthreshold swings of $\sim 60 \text{ mV/dec}$, a $I_{\text{on}}/I_{\text{off}}$ of $> 10^6$ at room temperature (others have shown $I_{\text{on}}/I_{\text{off}}$ of $> 10^7$ in WSe₂ and MoS₂), and high $I_{\text{on}} \sim 300 \mu\text{A}/\mu\text{m}$ [58, 114, 66, 115]. Undoped samples have shown to have room temperature mobility of an order of magnitude less than the doped counterparts [116, 115]. Note that these values are not the theoretical limits, but rather represent a current state of where measurements can achieve. To further improve the mobilities measured at room temperature a further understanding of scattering mechanisms is needed. At room temperature phonon scattering limits the mobility, the mobility can be enhanced by doping, however, this introduces impurities and can have an adverse effect on the mobility. Understanding the performance limit at room temperature in monolayers (and few layers) is key to applications in which several TMDs are already being implemented, such as thin film transistor (TFT) and components of ICs like analog amplifiers, digital inverters, and memory transistors [117, 24, 118].

4.4 Conclusion

Overall, TMDs offer a wealth of opportunities in applications. In order to realize these proposed applications several challenges must be overcome, namely achieving low-resistance contacts and high mobility at room temperature. The approach of using degenerately doped contacts and hBN encapsulated devices to

lower the SBH and promote increased mobility has shown potential. In addition, the increased mobility that the success of this method would allow one to study quantum transport properties which will reveal many fundamental properties, such as quantum scattering times and effective masses.

References

- [1] J Koenigsberger and J Weiss. Über die thermoelektrischen effekte (thermokräfte, thomsonwärme) und die wärmeleitung in einigen elementen und verbindungen und über die experimentelle prüfung der elektronentheorien. *Annalen der Physik*, 340(6):1–46, 1911.
- [2] G. Busch. Early history of the physics and chemistry of semiconductors-from doubts to fact in a hundred years. *European Journal of Physics*, 10:254–264, oct 1989.
- [3] KARL Lark-Horovitz. The present state of physics. *Am. Assoc. Advancement Sci., Washington, DC*, page 57, 1954.
- [4] A. H. Wilson. The theory of electronic semi-conductors. *Proceedings of the Royal Society of London. Series A, Containing Papers of a Mathematical and Physical Character*, 133(822):458–491, 1931.
- [5] A. H. Wilson. The theory of electronic semi-conductors. ii. *Proceedings of the Royal Society of London. Series A, Containing Papers of a Mathematical and Physical Character*, 134(823):277–287, 1931.
- [6] Donald A. Neaman. *Semiconductor Physics and Devices: Basic Principles*. McGraw-Hill, New York, NY, 3 edition, 2003.
- [7] Lidia Lukasiak and Andrzej Jakubowski. History of semiconductors. *Journal of Telecommunications and information technology*, pages 3–9, 2010.
- [8] Jack S. Kilby. Miniaturized electronic circuits. United States Patent Office, 1959. U.S. Patent 3,138,743, issued June 1964.
- [9] G. Moore. Cramming more components onto integrated circuits. *Electronics*, 38(8), 1965.
- [10] Peter Clarke. Intel enters billion-transistor processor era, October 2005. [Online; 13 accessed-December-2015].
- [11] James D. Meindl, Qiang Chen, and Jeffrey A. Davis. Limits on silicon nanoelectronics for terascale integration. *Science*, 293(5537):2044–2049, 2001.
- [12] Max Schulz. The end of the road for silicon? *Nature*, 399:729–730, 1999.
- [13] Joshua Golden, Melissa McMillan, Robert T Downs, Grethe Hystad, Ian Goldstein, Holly J Stein, Aaron Zimmerman, Dimitri A Sverjensky, John T Armstrong, and Robert M Hazen. Rhenium variations in molybdenite (mos 2): Evidence for progressive subsurface oxidation. *Earth and Planetary Science Letters*, 366:1–5, 2013.
- [14] Benjamin C Brodie. On the atomic weight of graphite. *Philosophical Transactions of the Royal Society of London*, pages 249–259, 1859.
- [15] H. W. Kroto, J. R. Heath, S. C. O’Brien, R. F. Curl, and R. E. Smalley. C60: Buckminsterfullerene. *Nature*, 318:162–163, 1985.

- [16] Ruben Mas-Balleste, Cristina Gomez-Navarro, Julio Gomez-Herrero, and Felix Zamora. 2d materials: to graphene and beyond. *Nanoscale*, 3:20–30, 2011.
- [17] Sumio Iijima. Helical microtubules of graphitic carbon. *Nature*, 354:56–58, 1991.
- [18] K. S. Novoselov, A. K. Geim, S. V. Morozov, D. Jiang, Y. Zhang, S. V. Dubonos, I. V. Grigorieva, and A. A. Firsov. Electric field effect in atomically thin carbon films. *Science*, 306(5696):666–669, 2004.
- [19] A. K. Geim and K. S. Novoselov. The rise of graphene. *Nature Materials*, 6:183–191, 2007.
- [20] K.S. Novoselov, A. K. Geim, S.V. Morozov, D. Jiang, M.I. Katsnelson, I.V. Grigorieva, S.V. Dubonos, and A.A. Firsov. Two-dimensional gas of massless dirac fermions in graphene. *Nature*, 438:197–200, 2005.
- [21] L. Zhang, Y. Zhang, J. Camacho, M. Khodas, and I. Zaliznyak. The experimental observation of quantum hall effect of l=3 chiral quasiparticles in trilayer graphene. *Nat. Phys.*, 7:953–957, 2011.
- [22] J. R. Williams, L. DiCarlo, and C. M. Marcus. Quantum hall effect in a gate-controlled p-n junction of graphene. *Science*, 317(5838):638–641, 2007.
- [23] Simone Bertolazzi, Jacopo Brivio, and Andras Kis. Stretching and breaking of ultrathin mos2. *ACS Nano*, 5(12):9703–9709, 2011. PMID: 22087740.
- [24] Deji Akinwande, Nicholas Petron, and James Hone. Two-dimensional flexible nanoelectronics. *Nature Communications*, 5, 2014.
- [25] A. Dargys and J. Kundrotas. *Handbook on physical properties of Ge, Si, GaAs, InP*. Science and Encyclopedia Publishers, Vilnius, Lithuania, 1994.
- [26] Ioffe Institute Database. Electrical properties of silicon. <http://www.ioffe.rssi.ru/SVA/NSM/Semicond/Si/electric.htm> [Online; Accessed 1 Feb. 2016].
- [27] K.S. Novoselov and A.K. Geim. The rise of graphene. *Nature Materials*, 6:183–191, 2007.
- [28] Berkley Labs. Bilayer graphene gets a bandgap, June 2009. [Online; 23 accessed-December-2015].
- [29] P. R. Wallace. The band theory of graphite. *Phys. Rev.*, 71:622–634, May 1947.
- [30] Mingsheng Xu, Tao Liang, Minmin Shi, and Hongzheng Chen. Graphene-like two-dimensional materials. *Chemical Reviews*, 113(5):3766–3798, 2013. PMID: 23286380.
- [31] F.N. Xia, T. Mueller, Y.M. Lin, A. Valdes-Garcia, and P. Avouris. Ultrafast graphene photodetector. *Nat. Nanotechnol.*, 4:839–843, 2009.
- [32] Feng Wang, Yuanbo Zhang, Chuanshan Tian, Caglar Girit, Alex Zettl, Michael Crommie, and Y. Ron Shen. Gate-variable optical transitions in graphene. *Science*, 320(5873):206–209, 2008.
- [33] T.J. Echtermeyer, L. Britnell, P.K. Jasnos, A. Lombardo, R.V. Gorbachev, A.N. Grigorenko, A.K. Geim, A.C. Ferrari, and K.S. Novoselov. Strong plasmonic enhancement of photovoltage in graphene. *Nat. Commun.*, 2:458, 2011.
- [34] Kyozaburo Takeda and Kenji Shiraishi. Theoretical possibility of stage corrugation in si and ge analogs of graphite. *Phys. Rev. B*, 50:14916–14922, Nov 1994.
- [35] S. Cahangirov, M. Topsakal, E. Aktürk, H. Şahin, and S. Ciraci. Two- and one-dimensional honeycomb structures of silicon and germanium. *Phys. Rev. Lett.*, 102:236804, Jun 2009.

- [36] R. F. Frindt and A. D. Yoffe. Physical properties of layer structures: Optical properties and photoconductivity of thin crystals of molybdenum disulphide. *Proceedings of the Royal Society of London A: Mathematical, Physical and Engineering Sciences*, 273(1352):69–83, 1963.
- [37] R. Fivaz and E. Mooser. Mobility of charge carriers in semiconducting layer structures. *Phys. Rev.*, 163:743–755, Nov 1967.
- [38] L. F. Mattheiss. Band structures of transition-metal-dichalcogenide layer compounds. *Phys. Rev. B*, 8:3719–3740, Oct 1973.
- [39] J.A. Wilson and A.D. Yoffe. The transition metal dichalcogenides discussion and interpretation of the observed optical, electrical and structural properties. *Advances in Physics*, 18(73):193–335, 1969.
- [40] AF Wells. Structural inorganic chemistry oxford univ. press, 1984.
- [41] B. Radisavljevic, A. Radenovic, J. Brivio, V. Giacometti, and A. Kis. Single-layer mos2 transistors. *Nat. Nano.*, 6:147–150, 2011.
- [42] Murong Lang, Liang He, Faxian Xiu, Xinxin Yu, Jianshi Tang, Yong Wang, Xufeng Kou, Wanjun Jiang, Alexei V. Fedorov, and Kang L. Wang. Revelation of topological surface states in bi₂se₃ thin films by in situ al passivation. *ACS Nano*, 6(1):295–302, 2012. PMID: 22147687.
- [43] Hong Bin Zhang, Hai Lin Yu, Ding Hua Bao, Shu Wei Li, Cheng Xin Wang, and Guo Wei Yang. Magnetoresistance switch effect of a sn-doped bi₂te₃ topological insulator. *Advanced Materials*, 24(1):132–136, 2012.
- [44] Wenjie Xie, Xinfeng Tang, Yonggao Yan, Qingjie Zhang, and Terry M. Tritt. Unique nanostructures and enhanced thermoelectric performance of melt-spun bisbte alloys. *Applied Physics Letters*, 94(10):–, 2009.
- [45] F. R. Gamble and B. G. Silbernagel. Anisotropy of the proton spinlattice relaxation time in the superconducting intercalation complex tas₂(nh₃): Structural and bonding implications. *The Journal of Chemical Physics*, 63(6):2544–2552, 1975.
- [46] Rui Cheng, Dehui Li, Hailong Zhou, Chen Wang, Anxiang Yin, Shan Jiang, Yuan Liu, Yu Chen, Yu Huang, and Xiangfeng Duan. Electroluminescence and photocurrent generation from atomically sharp wse₂/mos2 heterojunction p–n diodes. *Nano letters*, 14(10):5590–5597, 2014.
- [47] Hiram J Conley, Bin Wang, Jed I Ziegler, Richard F Haglund Jr, Sokrates T Pantelides, and Kirill I Bolotin. Bandgap engineering of strained monolayer and bilayer mos2. *Nano letters*, 13(8):3626–3630, 2013.
- [48] Seunghyun Lee and Zhaohui Zhong. Nanoelectronic circuits based on two-dimensional atomic layer crystals. *Nanoscale*, 6(22):13283–13300, 2014.
- [49] Andrea Splendiani, Liang Sun, Yuanbo Zhang, Tianshu Li, Jonghwan Kim, Chi-Yung Chim, Giulia Galli, and Feng Wang. Emerging photoluminescence in monolayer mos2. *Nano letters*, 10(4):1271–1275, 2010.
- [50] Yoichi Kubota, Kenji Watanabe, Osamu Tsuda, and Takashi Taniguchi. Deep ultraviolet light-emitting hexagonal boron nitride synthesized at atmospheric pressure. *Science*, 317(5840):932–934, 2007.
- [51] Ki Kang Kim, Allen Hsu, Xiaoting Jia, Soo Min Kim, Yumeng Shi, Mario Hofmann, Daniel Nezich, Joaquin F Rodriguez-Nieva, Mildred Dresselhaus, Tomas Palacios, et al. Synthesis of monolayer hexagonal boron nitride on cu foil using chemical vapor deposition. *Nano letters*, 12(1):161–166, 2011.

- [52] Li Song, Lijie Ci, Hao Lu, Pavel B Sorokin, Chuanhong Jin, Jie Ni, Alexander G Kvashnin, Dmitry G Kvashnin, Jun Lou, Boris I Yakobson, et al. Large scale growth and characterization of atomic hexagonal boron nitride layers. *Nano letters*, 10(8):3209–3215, 2010.
- [53] Kin Fai Mak, Changgu Lee, James Hone, Jie Shan, and Tony F Heinz. Atomically thin mos 2: a new direct-gap semiconductor. *Physical Review Letters*, 105(13):136805, 2010.
- [54] E Gourmelon, O Lignier, H Hadouda, G Couturier, JC Bernede, J Tedd, J Pouzet, and J Salardenne. Ms 2 (m= w, mo) photosensitive thin films for solar cells. *Solar energy materials and solar cells*, 46(2):115–121, 1997.
- [55] E Fortin and WM Sears. Photovoltaic effect and optical absorption in mos 2. *Journal of Physics and Chemistry of Solids*, 43(9):881–884, 1982.
- [56] Agnieszka Kuc, Nourdine Zibouche, and Thomas Heine. Influence of quantum confinement on the electronic structure of the transition metal sulfide t s 2. *Physical Review B*, 83(24):245213, 2011.
- [57] Yandong Ma, Ying Dai, Meng Guo, Chengwang Niu, Jibao Lu, and Baibiao Huang. Electronic and magnetic properties of perfect, vacancy-doped, and nonmetal adsorbed mose 2, mote 2 and ws 2 monolayers. *Physical Chemistry Chemical Physics*, 13(34):15546–15553, 2011.
- [58] Hui Fang, Steven Chuang, Ting Chia Chang, Kuniharu Takei, Toshitake Takahashi, and Ali Javey. High-performance single layered wse2 p-fets with chemically doped contacts. *Nano letters*, 12(7):3788–3792, 2012.
- [59] Saptarshi Das and Joerg Appenzeller. Wse2 field effect transistors with enhanced ambipolar characteristics. *Applied Physics Letters*, 103(10):103501, 2013.
- [60] Han Liu, Adam T Neal, and Peide D Ye. Channel length scaling of mos2 mosfets. *ACS nano*, 6(10):8563–8569, 2012.
- [61] Saptarshi Das, Hong-Yan Chen, Ashish Verma Penumatcha, and Joerg Appenzeller. High performance multilayer mos2 transistors with scandium contacts. *Nano letters*, 13(1):100–105, 2012.
- [62] Cheng Gong, Luigi Colombo, Robert M Wallace, and Kyeongjae Cho. The unusual mechanism of partial fermi level pinning at metal–mos2 interfaces. *Nano letters*, 14(4):1714–1720, 2014.
- [63] Joonki Suh, Tae-Eon Park, Der-Yuh Lin, Deyi Fu, Joonsuk Park, Hee Joon Jung, Yabin Chen, Changhyun Ko, Chaun Jang, Yinghui Sun, et al. Doping against the native propensity of mos2: Degenerate hole doping by cation substitution. *Nano letters*, 14(12):6976–6982, 2014.
- [64] Andre K Geim and Irina V Grigorieva. Van der waals heterostructures. *Nature*, 499(7459):419–425, 2013.
- [65] Mojtaba Farmanbar and Geert Brocks. Controlling the schottky barrier at mos 2/metal contacts by inserting a bn monolayer. *Physical Review B*, 91(16):161304, 2015.
- [66] Rajesh Kappera, Damien Voiry, Sibel Ebru Yalcin, Brittany Branch, Gautam Gupta, Aditya D Mohite, and Manish Chhowalla. Phase-engineered low-resistance contacts for ultrathin mos2 transistors. *Nature materials*, 13(12):1128–1134, 2014.
- [67] Mojtaba Farmanbar and Geert Brocks. Ohmic contacts to 2d semiconductors through van der waals bonding. *arXiv preprint arXiv:1601.02163*, 2016.
- [68] Robert W Keyes. The electrical properties of black phosphorus. *Physical Review*, 92(3):580, 1953.
- [69] Y Maruyama, S Suzuki, K Kobayashi, and S Tanuma. Synthesis and some properties of black phosphorus single crystals. *Physica B+ C*, 105(1):99–102, 1981.

- [70] Vy Tran, Ryan Soklaski, Yufeng Liang, and Li Yang. Layer-controlled band gap and anisotropic excitons in few-layer black phosphorus. *Phys. Rev. B*, 89:235319, Jun 2014.
- [71] Likai Li, Yijun Yu, Guo Jun Ye, Qingqin Ge, Xuedong Ou, Hua Wu, Donglai Feng, Xian Hui Chen, and Yuanbo Zhang. Black phosphorus field-effect transistors. *Nature nanotechnology*, 9(5):372–377, 2014.
- [72] Steven P Koenig, Rostislav A Doganov, Henrik Schmidt, AH Castro Neto, and Barbaros Ozyilmaz. Electric field effect in ultrathin black phosphorus. *Applied Physics Letters*, 104(10):103106, 2014.
- [73] Fengnian Xia, Han Wang, and Yichen Jia. Rediscovering black phosphorus as an anisotropic layered material for optoelectronics and electronics. *Nature communications*, 5, 2014.
- [74] Likai Li, Guo Jun Ye, Vy Tran, Ruixiang Fei, Guorui Chen, Huichao Wang, Jian Wang, Kenji Watanabe, Takashi Taniguchi, Li Yang, et al. Quantum oscillations in a two-dimensional electron gas in black phosphorus thin films. *Nature nanotechnology*, 2015.
- [75] Rino Choi, Chang Seok Kang, Hag-Ju Cho, Young-Hee Kim, Mohammad S. Akbar, and Jack C. Lee. Effects of high temperature forming gas anneal on the characteristics of metal-oxide-semiconductor field-effect transistor with hfo₂ gate stack. *Applied Physics Letters*, 84(24):4839–4841, 2004.
- [76] Yuan Huang, Eli Sutter, Norman N. Shi, Jiabao Zheng, Tianzhong Yang, Dirk Englund, Hong-Jun Gao, and Peter Sutter. Reliable Exfoliation of Large-Area High-Quality Flakes of Graphene and Other Two-Dimensional Materials. *ACS Nano*, 0(0):null, 0. PMID: 26336975.
- [77] C. Kittel. *Introduction to Solid State Physics*. Wiley, Hoboken, N. J., 8 edition, 2005.
- [78] Ernst Moritz Arndt Universität Greifswald: Soft Matter and Biophysics. AFM (Atomic Force Microscope, 2015. [Online; Accessed: 22, Jan. 2016].
- [79] Joe Nabity. NPGS: Nanometer Pattern Generation System, January 2016. [Online; Accessed: 26, Jan. 2016].
- [80] Xu Cui, Gwan-Hyoung Lee, Young Duck Kim, Ghidewon Arefe, Pinshane Y Huang, Chul-Ho Lee, Daniel A Chenet, Xian Zhang, Lei Wang, Fan Ye, et al. Multi-terminal transport measurements of mos2 using a van der waals heterostructure device platform. *Nature nanotechnology*, 2015.
- [81] Kristen Kaasbjerg, Kristian S Thygesen, and Karsten W Jacobsen. Phonon-limited mobility in n-type single-layer mos 2 from first principles. *Physical Review B*, 85(11):115317, 2012.
- [82] Steven Chuang, Corsin Battaglia, Angelica Azcatl, Stephen McDonnell, Jeong Seuk Kang, Xingtian Yin, Mahmut Tosun, Rehan Kapadia, Hui Fang, Robert M Wallace, et al. Mos2 p-type transistors and diodes enabled by high work function mox contacts. *Nano letters*, 14(3):1337–1342, 2014.
- [83] Dieter K. Schroder. *Semiconductor Material and Device Characterization*. John Wiley and Sons, Inc., Hoboken, New Jersey, 3rd edition, 2006.
- [84] Hsun-Jen Chuang, Bhim Prasad Chamlagain, Michael Koehler, Meeghage Madusanka Perera, Jia-qi Yang, David Mandrus, David Tomanek, and Zhixian Zhou. Low-resistance 2d/2d ohmic contacts: A universal approach to high-performance wse₂, mos₂, and mose₂ transistors. *Nano Letters*, 0(ja):null, 0.
- [85] Adrian Constantin Melissinos and Adrian C Melissinos. *Experiments in modern physics*, volume 114. Academic Press Orlando), 1966.
- [86] Thurber W.R. NIST: Hall effect measurements, Nov. 2011. [Online; Accessed: 26, Jan. 2016].

- [87] Nobelprize.org. Press release: The 1998 nobel prize in physics, 2016. [Online; Accessed: 26, Jan. 2016].
- [88] NR Pradhan, D Rhodes, S Memaran, JM Poumirol, D Smirnov, S Talapatra, S Feng, N Pereira-Lopez, AL Elias, M Terrones, et al. Hall and field-effect mobilities in few layered p-wse2 field-effect transistors. *Scientific reports*, 5, 2015.
- [89] A. F. Stassen, R. W. I. de Boer, N. N. Iosad, and A. F. Morpurgo. Influence of the gate dielectric on the mobility of rubrene single-crystal field-effect transistors. *Applied Physics Letters*, 85:3899, oct 2004.
- [90] Britton W. H. Baugher, Hugh O. H. Churchill, Yafang Yang, and Pablo Jarillo-Herrero. Intrinsic electronic transport properties of high-quality monolayer and bilayer mos2. *Nano Letters*, 13(9):4212–4216, 2013. PMID: 23930826.
- [91] Tsuneya Ando, Alan B Fowler, and Frank Stern. Electronic properties of two-dimensional systems. *Reviews of Modern Physics*, 54(2):437, 1982.
- [92] Neil W Ashcroft, N David Mermin, and Sergio Rodriguez. Solidstatephysics. *American Journal of Physics*, 46(1):116–117, 1978.
- [93] K. v. Klitzing, G. Dorda, and M. Pepper. New method for high-accuracy determination of the fine-structure constant based on quantized hall resistance. *Phys. Rev. Lett.*, 45:494–497, Aug 1980.
- [94] M. O. Goerbiger. Quantum Hall Effects. *ArXiv e-prints*, sep 2009. Provided by the SAO/NASA Astrophysics Data System.
- [95] J.R. Hook and E. Hall, H. *Solid State Physics*. Wiley, West Sussex, England, 2 edition, 1991.
- [96] Lev Davidovich Landau and Evgenii Mikhailovich Lifshitz. *Quantum mechanics: non-relativistic theory*, volume 3. Addison-Wesley, Reading, MA., 1965.
- [97] Jun John Sakurai and Jim J Napolitano. *Modern quantum mechanics*. Addison-Wesley, Reading, MA., 1994.
- [98] LD Landau. Diamagnetismus der metalle. *Zeitschrift für Physik*, 64(9-10):629–637, 1930.
- [99] M. A. Paalanen, D. C. Tsui, and A. C. Gossard. Quantized hall effect at low temperatures. *Phys. Rev. B*, 25:5566–5569, Apr 1982.
- [100] Klaus von Klitzing. The quantized hall effect. *Rev. Mod. Phys.*, 58:519–531, Jul 1986.
- [101] Hideo Aoki and Tsuneya Ando. Universality of quantum hall effect: Topological invariant and observable. *Phys. Rev. Lett.*, 57:3093–3096, Dec 1986.
- [102] L Bliek. Present understanding of the quantum hall effect. *Metrologia*, 25(2):67, 1988.
- [103] LV Shubnikov and WJ de Haas. Leiden commun. 207a (1930). *Proc. Netherlands R. Acad. Sci*, 33:130–163, 1930.
- [104] D. E. Soule, J. W. McClure, and L. B. Smith. Study of the shubnikov-de haas effect. determination of the fermi surfaces in graphite. *Phys. Rev.*, 134:A453–A470, Apr 1964.
- [105] R Peierls. On the theory of the diamagnetism of conduction electrons. ii strong magnetic fields. *Z. Phys*, 81:186–194, 1933.
- [106] LD Landau. See appendix to d. shoenberg. In *Proc. Roy. Soc. A*, volume 170, page 341, 1939.
- [107] David Shoenberg. *Magnetic oscillations in metals*. Cambridge University Press, 1984.

- [108] Sankar Das Sarma and Aron Pinczuk. Perspectives in quantum hall effects: Novel quantum liquids in low-dimensional semiconductor structures. *Perspectives in Quantum Hall Effects: Novel Quantum Liquids in Low-Dimensional Semiconductor Structures*, by Sankar Das Sarma (Editor), Aron Pinczuk (Editor), pp. 446. ISBN 0-471-11216-X. Wiley-VCH, November 1996., 1, 1996.
- [109] A. Tsukazaki, A. Ohtomo, T. Kita, Y. Ohno, H. Ohno, and M. Kawasaki. Quantum Hall Effect in Polar Oxide Heterostructures. *Science*, 315:1388–, mar 2007.
- [110] Nathaniel Gillgren, Darshana Wickramaratne, Yanmeng Shi, Tim Espiritu, Jiawei Yang, Jin Hu, Jiang Wei, Xue Liu, Zhiqiang Mao, Kenji Watanabe, Takashi Taniguchi, Marc Bockrath, Yafis Barlas, Roger K Lake, and Chun Ning Lau. Gate tunable quantum oscillations in air-stable and high mobility few-layer phosphorene heterostructures. *2D Materials*, 2(1):011001, 2015.
- [111] Xiaodong Li, Jeffrey T Mullen, Zhenghe Jin, Kostyantyn M Borysenko, M Buongiorno Nardelli, and Ki Wook Kim. Intrinsic electrical transport properties of monolayer silicene and mos 2 from first principles. *Physical Review B*, 87(11):115418, 2013.
- [112] Banimir Radisavljevic, Aleksandra Radenovic, Jacopo Brivio, V Giacometti, and A Kis. Single-layer mos2 transistors. *Nature nanotechnology*, 6(3):147–150, 2011.
- [113] Rajesh Kappera, Damien Voiry, Sibel Ebru Yalcin, Wesley Jen, Muhamrem Acerce, Sol Torrel, Brittany Branch, Sidong Lei, Weibing Chen, Sina Najmaei, et al. Metallic 1t phase source/drain electrodes for field effect transistors from chemical vapor deposited mos2. *APL Materials*, 2(9):092516, 2014.
- [114] Wei Liu, Jiahao Kang, Deblina Sarkar, Yasin Khatami, Debdeep Jena, and Kaustav Banerjee. Role of metal contacts in designing high-performance monolayer n-type wse2 field effect transistors. *Nano letters*, 13(5):1983–1990, 2013.
- [115] Saptarshi Das, Richard Gulotty, Anirudha V Sumant, and Andreas Roelofs. All two-dimensional, flexible, transparent, and thinnest thin film transistor. *Nano letters*, 14(5):2861–2866, 2014.
- [116] Song-Lin Li, Katsunori Wakabayashi, Yong Xu, Shu Nakaharai, Katsuyoshi Komatsu, Wen-Wu Li, Yen-Fu Lin, Alex Aparecido-Ferreira, and Kazuhito Tsukagoshi. Thickness-dependent interfacial coulomb scattering in atomically thin field-effect transistors. *Nano letters*, 13(8):3546–3552, 2013.
- [117] Ganesh R Bhimanapati, Zhong Lin, Vincent Meunier, Yeonwoong Jung, Judy Cha, Saptarshi Das, Di Xiao, Youngwoo Son, Michael S Strano, Valentino R Cooper, et al. Recent advances in two-dimensional materials beyond graphene. *ACS nano*, 9(12):11509–11539, 2015.
- [118] Hee Sung Lee, Sung-Wook Min, Min Kyu Park, Young Tack Lee, Pyo Jin Jeon, Jae Hoon Kim, Sunmin Ryu, and Seongil Im. Mos2 nanosheets for top-gate nonvolatile memory transistor channel. *Small*, 8(20):3111–3115, 2012.

Appendices

2DEG two-dimensional electron gas

2DES two-dimensional electron system

2DHG two-dimensional hole gas

AFM atomic force microscopy

Au gold

BJD Bell Jar deposition

BP black phosphorus

DI deionized water

DFT density functional theory

EBL electron beam lithography

IC integrated circuit

IPA isopropanol

IQHE integer quantum Hall effect

MEK methyl ethyl ketone

MFM magnetic force microscopy

MIBK methyl isobutyl ketone

Mo molybdenum

MoS₂ molybdenum disulfide

N₂ nitrogen

Nb niobium

Ni nickel

NPGS Nanometer Pattern Generation System

PC polycarbonate

PDMS polydimethylsiloxane

PMMA polymethyl methacrylate

PPMS physical property measurement system

QHE quantum hall effect

Re rhenium

S sulfur

SB Schottky barrier

SBH Schottky barrier height

Se selenium

SEM scanning electron microscope

SdH Shubnikov-de Haas

SiO₂ silicon dioxide

STM scanning tunneling microscopy

Te tellurium

TEM transmission electron microscopy

TFT thin film transistor

Ti titanium

TLM transmission line model

TMD transition metal dichalcogenides

V vanadium

W tungsten

WS₂ tungsten disulfide

WSe₂ tungsten diselenide

ACKNOWLEDGEMENTS

Acknowledgements here...